To appear in *Astrophys. J. Supp. Ser.*

Dielectronic Recombination in Photoionized Gas. II. Laboratory Measurements for Fe XVIII and Fe XIX

D. W. Savin and S. M. Kahn
Department of Physics and Columbia Astrophysics Laboratory, Columbia University, New York, NY 10027, USA

J. Linkemann, A. A. Saghiri, M. Schmitt, M. Grieser, R. Repnow, D. Schwalm, and A. Wolf
Max-Planck-Institut für Kernphysik, D-69117 Heidelberg, Germany
and Physikalisches Institut der Universität Heidelberg, 69120 Heidelberg, Germany

T. Bartsch, C. Brandau, A. Hoffknecht, A. Müller, and S. Schippers
Institut für Kernphysik, Strahlenzentrum der Justus-Liebig-Universität, D-35392 Giessen, Germany

M. H. Chen
Lawrence Livermore National Laboratory, Livermore, CA 94550, USA

and

N. R. Badnell
Department of Physics and Applied Physics, University of Strathclyde, Glasgow, G4 0NG, United Kingdom

ABSTRACT

In photoionized gases with cosmic abundances, dielectronic recombination (DR) proceeds primarily via $nlj \rightarrow nl'j'$ core excitations ($\Delta n = 0$ DR). We have measured the resonance strengths and energies for Fe XVIII to Fe XVII and Fe XIX to Fe XVIII $\Delta n = 0$ DR. Using our measurements, we have calculated the Fe XVIII and Fe XIX $\Delta n = 0$ DR rate coefficients. Significant discrepancies exist between our inferred rates and those of published calculations. These calculations overestimate the DR rates by factors of ~ 2 or underestimate it by factors of ~ 2 to orders of magnitude, but none are in good agreement with our results. Almost all published DR rates for modeling cosmic plasmas are computed using the same theoretical techniques as the above-mentioned calculations. Hence, our measurements call into question all theoretical $\Delta n = 0$ DR rates used for ionization balance calculations of cosmic plasmas. At temperatures where the Fe XVIII and Fe XIX fractional abundances are predicted to peak in photoionized gases of cosmic abundances, the theoretical rates underestimate the Fe

XVIII DR rate by a factor of ~ 2 and overestimate the Fe XIX DR rate by a factor of ~ 1.6. We have carried out new multiconfiguration Dirac-Fock and multiconfiguration Breit-Pauli calculations which agree with our measured resonance strengths and rate coefficients to within typically better than $\lesssim 30\%$. We provide a fit to our inferred rate coefficients for use in plasma modeling. Using our DR measurements, we infer a factor of ~ 2 error in the Fe XX through Fe XXIV $\Delta n = 0$ DR rates. We investigate the effects of this estimated error for the well-known thermal instability of photoionized gas. We find that errors in these rates cannot remove the instability, but they do dramatically affect the range in parameter space over which it forms.

Subject headings: atomic data — atomic processes — galaxies: active — instabilities — X-rays: general

1. Introduction

Photoionized gases form in planetary nebulae, H II regions, stellar winds, cold novae shells, active galactic nuclei, X-ray binaries, and cataclysmic variables. In such gases the electron temperature T_e at which an ion forms (Kallman et al. 1996) is far below that where the ion forms in coronal equilibrium (Arnaud & Rothenflug 1985; Arnaud & Raymond 1992). As a result, the dominant electron-ion recombination processes are radiative recombination (RR) and low temperature dielectronic recombination via $nlj \rightarrow nl'j'$ excitations of core electrons ($\Delta n = 0$ DR). Also, X-ray line emission is produced not by electron impact excitation but by RR and DR (Liedahl et al. 1990; Kallman et al. 1996)

Recent *ASCA* observations of the low-mass X-ray pulsar 4U 1626-67 (Angelini et al. 1995) and the X-ray binary Cygnus X-3 (Liedahl & Paerels 1996) have spectroscopically confirmed the low T_e of photoionized gas and demonstrated some of the unique properties of such gas. The soon-to-be-launched satellites *AXAF*, *XMM*, and *Astro-E* are expected to collect spectra which will reveal, in even greater detail, the X-ray properties of photoionized gases. Of particular interest will be $n \geq 3 \rightarrow n = 2$ line emission of Fe XVII to Fe XXIV (the iron L-shell ions) which dominates the $0.7 - 2.0$ keV (6-18 Å) bandpass.

Iron L-shell ions form over a wide range of physical conditions and are expected to provide many valuable plasma diagnostics (Kahn & Liedahl 1995). However, the accuracies of these diagnostics will be limited by uncertainties in the relevant atomic data. This will be an issue especially for low temperature DR rate coefficients of iron L ions. These rates are theoretically and computationally challenging as they require accurate energy levels for ions with partially-filled shells and involve calculating a near-infinite number of states. The challenge of these calculations can be seen by the spread in the computed $\Delta n = 0$ DR rates for Fe XVIII to Fe XVII and Fe XIX to Fe XVIII. Existing theoretical Fe XVIII (Roszman 1987a; Chen 1988; Dasgupta & Whitney

1990) and Fe XIX (Roszman 1987b; Dasgupta & Whitney 1994) rates differ by factors of 2 to 4 over the temperature ranges where these ions are predicted to form in photoionized gas of cosmic abundances (Kallman et al. 1996).

DR begins when a free electron excites an ion and is simultaneously captured. This state d may autoionize. DR is complete when d emits a photon which reduces the energy of the recombined system to below its ionization limit. Conservation of energy requires

$$E_k = \Delta E - E_b, \tag{1}$$

where E_k is the kinetic energy of the incident electron, ΔE the excitation energy of the core electron in the presence of the incident electron, and E_b the binding energy released when the free electron is captured. Because ΔE and E_b are quantized, DR is a resonance process.

The strength of a DR resonance is given by the integral of the resonance cross section over energy. In the isolated resonance approximation, the integrated strength of a particular DR resonance $\hat{\sigma}_d$ can be approximated as (Kilgus et al. 1992)

$$\hat{\sigma}_d = \frac{h\mathcal{R}}{E_d}\pi a_0^2 \frac{g_d}{2g_i} \frac{A_a(d \to i) \sum_f A_r(d \to f)}{\sum_\kappa A_a(d \to \kappa) + \sum_{f'} A_r(d \to f')}. \tag{2}$$

Here h is the Planck constant; $\mathcal{R}$ is the Rydberg energy constant; E_d is the energy of resonance d; a_0 is the Bohr radius; g_d and g_i are the statistical weights of d and of the initial ion, respectively; A_a and A_r are the autoionization and radiative decay rates, respectively; $\sum_f$ is over all states stable against autoionization; $\sum_{f'}$ is over all states energetically below d; both $\sum_f$ and $\sum_{f'}$ may include cascades through lower-lying autoionizing states and ultimately to bound states; and $\sum_\kappa$ is over all states attainable by autoionization of d.

To address the needs for modeling photoionized gases, we are carrying out a series of experiments to measure the $\Delta n = 0$ DR rates for the iron L-shell ions. Measurements are performed using the heavy-ion Test Storage Ring (TSR) at the Max-Planck-Institute for Nuclear Physics in Heidelberg, Germany (Habs et al. 1989; Kilgus et al. 1992). In Savin et al. (1997), we gave a summary of our measurements for Fe XVIII. Here we present a more detailed analysis of those results as well as our new measurements for Fe XIX. Measurements have also been carried out for M-shell Fe XVI (Linkemann et al. 1995).

Fe XVIII is fluorinelike with a $2p_{3/2}$ hole and a ground state of ${}^2P_{3/2}$. Table 1 lists the energies (relative to the ground state) of all Fe XVIII levels in the $n = 2$ shell. Fe XVIII can undergo $\Delta n = 0$ DR via the capture channels

$$\mathrm{Fe}^{17+}(2s^2 2p^5[{}^2P_{3/2}]) + e^- \quad \to \left\{ \begin{array}{ll} \mathrm{Fe}^{16+}(2s^2 2p^5[{}^2P_{1/2}]nl) & (n = 18, \ldots, \infty) \\ \mathrm{Fe}^{16+}(2s 2p^6[{}^2S_{1/2}]nl) & (n = 6, \ldots, \infty). \end{array} \right. \tag{3}$$

The first channel involves the excitation of a $2p_{1/2}$ electron to the $2p_{3/2}$ subshell. This fills the $2p_{3/2}$ subshell, creates a hole in the $2p_{1/2}$ subshell, and leaves the ion core in a ${}^2P_{1/2}$ state. The second channel involves the excitation of a $2s_{1/2}$ electron to the $2p_{3/2}$ subshell. This fills the $2p_{3/2}$ subshell, creates a hole in the $2s_{1/2}$ subshell, and leaves the ion core in a ${}^2S_{1/2}$ state. The radiative stabilization of these autoionizing states to bound configurations of Fe XVII leads to DR resonances for collision energies between 0 and ~ 132 eV. The lowest energy $\Delta n = 1$ DR resonances occur for $E_k \sim 220$ eV.

Table 1 also lists the energies (relative to the ground state) of all Fe XIX levels in the $n = 2$ shell. Fe XIX is oxygenlike and can undergo $\Delta n = 0$ DR via a number of channels. Those channels which are strong enough for us to observe DR resonances are

$$\mathrm{Fe}^{18+}(2s^2 2p^4[{}^3P_2]) + e^- \rightarrow \begin{cases} \mathrm{Fe}^{17+}(2s^2 2p^4[{}^3P_0]nl) & (n = 22, \ldots, \infty) \\ \mathrm{Fe}^{17+}(2s^2 2p^4[{}^3P_1]nl) & (n = 20, \ldots, \infty) \\ \mathrm{Fe}^{17+}(2s^2 2p^4[{}^1D_2]nl) & (n = 15, \ldots, \infty) \\ \mathrm{Fe}^{17+}(2s^2 2p^4[{}^1S_0]nl) & (n = 11, \ldots, \infty) \\ \mathrm{Fe}^{17+}(2s 2p^5[{}^3P_2^o]nl) & (n = 7, \ldots, \infty) \\ \mathrm{Fe}^{17+}(2s 2p^5[{}^3P_1^o]nl) & (n = 7, \ldots, \infty) \\ \mathrm{Fe}^{17+}(2s 2p^5[{}^3P_0^o]nl) & (n = 6, \ldots, \infty). \end{cases} \quad (4)$$

Radiative stabilization of the Fe XVIII autoionizing states to bound configurations of Fe XVIII leads to measurable DR resonances for electron-ion collision energies between 0 and ~ 128 eV. The lowest energy $\Delta n = 1$ DR resonances occur for $E_k \sim 218$ eV.

In Section 2 we describe the experimental arrangement used to obtain the present results. Section 3 compares our measurements with published DR calculations. In Section 4 we discuss new theoretical calculations which we have carried out for comparison with our measurements, while Section 5 discusses the astrophysical implications of our results.

2. Experimental Technique

DR measurements are carried out by merging, in one of the straight sections of TSR, the circulating ion beam with an electron beam. After demerging, recombined ions are separated from the stored ions using a dipole magnet and directed onto a detector. The relative electron-ion collision energy can be precisely controlled and the recombination signal measured as a function of this energy. A detailed description of TSR (Habs et al. 1989) and the procedures used for DR measurements have been given elsewhere (Kilgus et al. 1992; Lampert et al. 1996). The experimental arrangement for our Fe XVIII measurements is discussed in Savin et al. (1997). Here we describe primarily the setup used for our Fe XIX results and mention only those details for Fe XVIII which were not discussed previously.

Negative ^{56}Fe ions are accelerated and stripped using a tandem accelerator and then further accelerated to 241 MeV and stripped to their final charge state of 18+. The ions are injected into TSR and accumulated using repeated multiturn-injection stacking techniques (Grieser et al. 1991) and electron cooling (Poth 1990). In this manner stored ion currents of $\sim 20-60$ μA are achieved. The storage lifetime is ~ 30 s. After stacking, the ions are electron cooled for ~ 5 s before data collection begins. This is long compared to the lifetime of the various metastable Fe XIX levels (Cheng, Kim, & Desclaux 1979), and the ions are assumed to be in their ground state when the DR measurements begin. The beam width, measured using a beam profile monitor (Hochadel et al. 1994), is $\sim 2-3$ mm after cooling.

The electrons are guided by a magnetic field of 41 mT and merged with the ions over a straight interaction region of length $L \sim 1.5$ m. For cooling, the electron velocity, v_e, is matched to that of the ions, v_i. The electron beam is adiabatically expanded before merging (from a diameter of ~ 0.95 to ~ 3.4 cm) to reduce its velocity spread perpendicular to the magnetic field (Pastuszka et al. 1996). The resulting energy distribution of the electrons is best described in the present experiment by an anisotropic Maxwellian distribution characterized by temperatures of $k_BT_\perp \sim 17$ meV and $k_BT_\| \sim 0.4$ meV which are, respectively, perpendicular and parallel to the confining magnetic field (and k_B is the Boltzmann constant). The electron density n_e varies between ~ 2.7 and 5.1×10^7 cm^{-3}.

For the Fe XIX measurements, the electron energy is chopped from cooling to a reference energy and then to the measurement energy. Each energy step is maintained for 25 ms. After waiting for 5 ms, data are acquired for the last 20 ms of each step. The reference energy is chosen so that RR and DR contribute insignificantly to the recombination signal. The recombination signal at the reference energy represents only the background caused by charge transfer (CT) of the ions with the rest gas in TSR. For the present results, the reference energy is ~ 1600 eV greater than the cooling energy (~ 2360 eV). This corresponds to a center-of-mass energy of ~ 170 eV. For the Fe XVIII measurements the same timing was used but there was no step to a reference energy, i.e. the electron energy was chopped only between cooling and measurement energy.

The relative electron-ion collision energies E are calculated using v_e (as determined using the calibrated electron acceleration voltage and accounting for space charge effects in the electron beam) and v_i in the overlap region. The resulting experimental energy scale was verified by comparing the measured DR resonance energies to the calculated resonance energies using

$$E_{nl} = \Delta E - \left(\frac{z}{n-\mu_l}\right)^2 \mathcal{R} \tag{5}$$

where z is the charge of the ion before recombination, n is the Rydberg level into which the free electron is captured, and μ_l is the quantum defect for the recombined ion. The quantum defect is to account for energy shifts of those l levels which have a significant overlap with the ion core and cannot be described using the uncorrected Rydberg formula. For high enough l levels this overlap is insignificant. Note that here the quantum defects are for recombined ions with an excited core, not one in the ground state

To verify the Fe XVIII energy scale we used Equation 5 to fit the measured resonance energies for a given Rydberg series (see Section 3). Only resonances for which μ_l is essentially 0 were used, and ΔE and $\mathcal{R}$ were fit for. For the Fe XVIII data we found relative differences between the measured and calculated resonance energies on the order of 2%. These differences could be traced to small deviations of the acceleration voltage from its calibrated values during the chopping cycles. In particular, on chopping from the lower-lying cooling energy to the measurement energy, the electron energy did not reach its desired value but remained below it by a small amount. To correct for these deviations we reduced the experimental energy scale by a factor of ~ 1.02. After this correction, a fit of the measured resonance energies, using Equation 5, yielded a value of $\mathcal{R}$ which matched its known value and values for ΔE which matched the spectroscopically measured energies of the Fe XVIII $2s^22p^5(^2P_{3/2}) - 2s^22p^5(^2P_{1/2})$ and $2s^22p^5(^2P_{3/2}) - 2s2p^6(^2S_{1/2})$ transitions (Sugar & Corliss 1985; Shirai et al. 1990). We also compared the measured energies for high-n, high-l DR resonances and those predicted by Equation 5. The uncertainty in the corrected energy scale is estimated to be $\lesssim 0.4\%$.

For the Fe XIX results, similar deviations of the acceleration voltage from its calibrated values are found. In particular, on chopping from the higher-lying reference energy to the measurement energy, the electron energy did not reach its desired value but stayed above it by a small amount. Technical reasons for the occurence of these voltage errors in the Fe XVIII and the Fe XIX runs (in contrast to earlier DR measurements at TSR) have been identified only during the course of the data reduction after the measurements had been completed. For the Fe XIX run the discrepancy between measured and calculated resonance energies was greatest for large energy differences between the reference and measurement energies and was noticed because the energies of the DR resonances for $v_i > v_e$ and for $v_i < v_e$ were not symmetric around $v_i = v_e$. The discrepancy became insignificant near the $^3P_2 -^3 P^o_{1,2}$ DR series limits. A small increase to the electron energy assumed in the data analysis symmeterized the DR resonance energies around $v_i = v_e$ but resulted in an overestimate of the energy scale.

To re-calibrate our Fe XIX energy scale we used Equation 5 to fit the measured resonance energies for a given Rydberg series (see Section 3). Only those levels were used for which μ_l is essentially 0, and ΔE and $\mathcal{R}$ were fit for. We then reduced the experimental energy scale by a factor of ~ 1.02 so the Rydberg value matched its known value and the inferred values for ΔE matched their spectroscopically measured energies of the Fe XIX $2s^22p^4(^3P_2) - 2s^22p^4(^3P_1)$, $2s^22p^4(^3P_2) - 2s^22p^4(^1D_2)$, $2s^22p^4(^3P_2) - 2s2p^5(^3P^o_2)$, and $2s^22p^4(^3P_2) - 2s2p^5(^3P^o_1)$ transitions (Sugar & Corliss 1985; Shirai et al. 1990). We also compared the measured energies for high-n, high-l DR resonances and those predicted by Equation 5. The uncertainty in the corrected energy scale is estimated to be $\lesssim 0.7\%$.

Toroidal magnets are used to merge the ion and electron beams, and after the straight interaction region to separate the beams again. For recombination measurements of Fe XVIII (Fe XIX), the motional electric field produced by the second toroidal magnet can field ionize electrons that after the DR process remain in Rydberg levels $n \gtrsim n_{cut1} = 145(132)$. Correction dipole magnets after the electron cooler can ionize electrons in Rydberg levels $n \gtrsim n_{cut2} = 143(130)$. For the Fe XVIII data the magnetic field strengths in the toroid and the correction dipoles were smaller than for the Fe XIX data. Downstream of the correction dipoles, recombined ions are separated from the stored ions using another dipole magnet and directed onto a fast scintillator, heavy-ion detector with an efficiency of $\gtrsim 95\%$ (Miersch et al. 1996). For the Fe XVIII data the magnetic field strength in this dipole magnet was larger than for the Fe XIX data. Electrons in Rydberg states with $n \gtrsim n_{cut3} = 56(63)$ can be field ionized by this magnet. However, during the ~ 5.1 m from the center of the cooler to the dipole magnet, electrons in high Rydberg levels can radiatively decay below the various values of n_{cut}. Using the $\sim 156(177)$ ns flight time of the ions, the fact that dielectronic capture occurs predominantly into $l \lesssim 8$, the hydrogenic formula for radiative lifetimes of Marxer & Spruch (1991), and the values of n_{cut1} to n_{cut3} for the Rydberg cutoffs of the toroid and dipole correction magnets, we estimate that DR into $n \lesssim n_{max} = 124(130)$ will radiatively decay below the different values of n_{cut}. The value of n_{max} determines the maximum quantum number of the DR-populated Rydberg level that can be detected in our experimental arrangement.

The measured recombination signal is the sum of RR, DR, and CT off the rest gas in the cooler. Recombination of Fe XVIII due to CT is taken into account by subtracting a constant count rate per ion such that the measured rate coefficient at 134 eV matches the very low theoretical RR rate at that energy (Lampert et al. 1996). Since the pressure in the cooler varies with the electron energy, there is a weak dependence of the CT signal on the measurement energy. Thus, the subtraction technique used for the Fe XVIII data can remove most but not all of the CT background signal. The remaining CT signal, however, is a smooth function of energy and can be readily subtracted out when extracting resonance strengths from the data.

The Fe XIX recombination signal rate R is calculated by subtracting the rate at the reference energy from the rate at measurement. Effects of slow pressure variations during the scanning of the measurement energy are therefore eliminated. Only a weak contribution due to CT remains in R due to small fast pressure variations associated with the chopping of the electron energy. The measured recombination rate coefficient α_L is given by $\alpha_L(E) = R\gamma^2/(Ln_eN_i/C)$ where N_i is the number of ions stored in the ring, $C = 55.4$ m the circumference of the ring, $\gamma^2 = [1-(v_i/c)^2]^{-1} \approx 1.01$, and c the speed of light. The measured rate coefficient is a convolution of the DR and RR cross sections with the experimental energy spread, which is best described by an anisotropic Maxwellian distribution in the co-moving frame of the electron beam (see above), sitting atop the residual CT background.

Peaks in the measured data $\alpha_L(E)$ are due to DR. As described in Section 3, resonance strengths can be extracted after subtracting a smooth background which is due to RR and CT. While this smooth contribution is dominated by RR at low collision energies, we are unable to extract reliable RR rate coefficients from the Fe XVIII and Fe XIX data due to remaining CT contributions in the measured signal rate.

Systematic uncertainties for the absolute DR rate coefficients are due to the ion current and electron density determinations, corrections for merging and demerging of the electron and ion beams, recombined ion detection efficiency, and uncertainties in the shape of the residual CT background. The total systematic uncertainty is estimated to be less than 20%. Relative uncertainties for comparing DR rate coefficients at different energies are estimated to be less than 10%. Uncertainties are quoted at a confidence level believed to be equivalent to a 90% counting statistics confidence level.

3. Results and Discussion

3.1. Measured Resonance Strengths, Energies, and Quantum Defects

Figures 1 and 2 show, respectively, our measured Fe XVIII to Fe XVII and Fe XIX to Fe XVIII $\Delta n = 0$ DR rate coefficients as a function of collision energy. The resonances seen in these figures are due to the convolution of the DR cross sections with the anisotropic Maxwellian electron distributions of the two experiments. Effects from the merging and de-merging of the electron and ion beams have been corrected for as described in Lampert et al. (1996). In Figure 1, at low energies DR of Fe XVIII via the fine structure ${}^2P_{3/2} - {}^2P_{1/2}$ core excitation can be seen. Similar behavior was observed in an earlier measurement on the isoelectronic Se XXVI (Lampert et al. 1996). For Fe XIX at low energies (Figure 2), DR via the fine structure ${}^3P_2 - {}^3P_1$ and ${}^3P_2 - {}^1D_2$ core excitations can clearly be seen. At high energies, resonances are visible due to ${}^2P_{3/2} - {}^2S_{1/2}$ excitations for Fe XVIII, and due to ${}^3P_2 - {}^3P^o_2$ and ${}^3P_2 - {}^3P^o_1$ excitations for Fe XIX.

Resonance strengths and energies have been extracted by fitting the measured resonances using the predicted asymmetric line shape (Kilgus et al. 1992) for energies below 13 eV for Fe XVIII and below 25 eV for Fe XIX. Above 13(25) eV, the asymmetry is insignificant and we have used Gaussian line shapes. Tables 2 and 3 list the extracted resonance energies and strengths for Fe XVIII DR via the ${}^2P_{3/2} - {}^2P_{1/2}$ and ${}^2P_{3/2} - {}^2S_{1/2}$ core excitations, respectively. Measured Fe XIX resonance energies and strengths are listed in Table 4. All energies quoted have been corrected as described in Section 2.

Using Equation 5 with the correct values of ΔE and $\mathcal{R}$ and the measured resonance energies in Tables 2, 3, and 4, we have determined the quantum defects for s, p, and d electrons of Fe XVII and for p and d electrons of Fe XVIII (Table 5). For Fe XVII, we do not use Fe XVIII DR resonances via the ${}^2P_{3/2} - {}^2S_{1/2}$ core excitation for capture into the $n = 6$ level. For Fe XVIII, we use only those $n \geq 8$ Fe XIX DR resonances for the ${}^3P_2 - {}^3P^o_1$ and ${}^3P_2 - {}^3P^o_2$ core excitations which are unblended. We do not use resonances due to capture into the $n \leq 6(7)$ level because the resonance structure is too complicated to be accurately approximated using Equation 5. For each ion we have determined quantum defects for two different excited core configurations. For a given value of l, one would expect different quantum defects for the different cores. However, due to the $\lesssim 0.4\%$ and $\lesssim 0.7\%$ accuracy of our energy scale for Fe XVIII and Fe XIX DR, respectively, we are unable to discern any difference. For example, the $\sim 10\%$ difference between the measured values of μ_d for Fe XVII yields an $\lesssim 0.2\%$ difference in calculated resonance energies.

Theodosiou, Inokuti, & Manson (1986) have calculated quantum defects for ions with a ground state core (Table 5). Their values are consistently lower than the experimental values for Fe XVII and in better agreement for Fe XVIII, but overall yield resonance energies which agree with the measured values to within the uncertainty of our energy scale. This suggests that $\Delta n = 0$ core excitations do not significantly affect quantum defects for outer electrons in $n \geq 7$ levels for Fe XVII and $n \geq 8$ levels for Fe XVII.

3.2. Inferred Maxwellian-Averaged Rate Coefficients and Comparison with Published Calculations

3.2.1. Fe XVIII

As shown in Savin et al. (1997), existing Fe XVIII $\Delta n = 0$ DR calculations do not account for DR via the $2p_{1/2} \rightarrow 2p_{3/2}$ (i.e., ${}^2P_{3/2} - {}^2P_{1/2}$) fine-structure core excitation. For comparison with published theory, we have calculated a Maxwellian-averaged Fe XVIII DR rate using only our measured ${}^2P_{3/2} - {}^2S_{1/2}$ DR resonance strengths and energies. This rate is shown in Figure 3 together with the theoretical results of Chen (1988), Roszman (1987), Dasgupta & Whitney (1990), and the Burgess (1965) formula using the oscillator strengths of Fuhr, Martin, & Wiese (1988).

Significant discrepancies exist between our inferred rate and the calculations of Chen and Roszman. The fully-relativistic, multiconfiguration Dirac Fock (MCDF) calculations by Chen underestimate the DR rate by a factor of ~ 1.5. This may be partly due to approximations which ignore DR for capture into Rydberg levels with $l > 8$ and partly due to the over-estimation of the resonance energies. Including these levels and reducing the resonance energies would increase the calculated DR rate. Chen carried out explicit calculations for $n \leq 20$ and thus included the effects of autoionization via a $2s2p^6({}^2S_{1/2})nl \rightarrow 2s^22p^5({}^2P_{1/2}) + e^-$ transition ($n \geq 18$).

The single-configuration, LS-coupling calculations by Roszman overestimate the DR rate by a factor of ~ 1.6 for $k_BT_e \gtrsim 40$ eV. This may be partly due to using LS-coupling which leaves out the $2s2p^6({}^2S_{1/2})nl \rightarrow 2s^22p^5({}^2P_{1/2}) + e^-$ autoionization channel. This opens up at $n = 18$ and would, if included, reduce the DR rate. The discrepancy may also be partly due to a possible error in the calculated resonance energies. This could also explain the low temperature behavior of Roszman's results. Below ~ 40 eV Roszman underestimates the ${}^2P_{3/2} - {}^2S_{1/2}$ DR rate because he calculated that DR via this channel becomes energetically possible at $n = 7$. Our experiment shows this channel, in fact, opens up for $n = 6$. Roszman also, like Chen, did not include contributions due to capture into $l > 8$ levels. This results in underestimating the DR rate. In short, the full reason for the discrepancy between Roszman's and our inferred rates is unclear. The differences between Chen's and Roszman's calculations may be partly related to differences between MCDF and single-configuration, LS-coupling methods.

The Burgess (1965) formula underestimates the DR rate for $k_BT_e \lesssim 80$ eV. This is due to setting all DR resonance energies to the threshold energy for the core excitation under consideration. This is valid only for DR into high n levels; and as noted by Burgess, himself, the formula is only applicable when recombination in high n levels dominates the DR process.

The agreement between our rate and the single-configuration, intermediate-coupling calculations of Dasgupta & Whitney is probably serendipitous. They carried out explicit calculations only for $n \leq 15$ and $l \leq 8$ and used extrapolation techniques for higher n levels. This leaves out the $2s2p^6(^2S_{1/2})nl \rightarrow 2s^22p^5(^2P_{1/2}) + e^-$ autoionization channel which results in an overestimation of the DR rate. Accounting for $l \leq 8$ results in an underestimate of the DR rate. The agreement may be due to the various approximations used roughly canceling out in the energy-averaged, total rate coefficient.

This case clearly illustrates that comparisons of only Maxwellian-averaged rate coefficients cannot be used to distinguish between different theoretical techniques. A detailed comparison between experimental and theoretical resonance strengths and energies is the only unambiguous way to verify the accuracy of DR rate coefficient calculations. This is now possible using high-resolution DR measurements carried out at heavy-ion storage rings (as will be illustrated in Section 4).

To obtain a total Fe XVIII to Fe XVII $\Delta n = 0$ DR rate coefficient, we have convolved all our measured resonance strengths and energies, including also the fine-structure excitation channel, with an isotropic Maxwellian electron distribution (Figure 4). The estimated total experimental uncertainty is less than 20%. The published theoretical DR rates are also shown in Figure 4. These rates all go rapidly to zero for $k_BT_e \lesssim 30$ eV because they have not accounted for DR via $2p_{1/2} \rightarrow 2p_{3/2}$ core excitations. The Burgess formula (1965) also does not account for this channel and goes rapidly to zero for low k_BT_e because the formula is valid only for core excitations connected to the ground state via an electric dipole transition. To sum up, at temperatures of $k_BT_e \sim 15$ eV, near where the fractional abundance of Fe XVIII is predicted to peak in a photoionized plasma of cosmic abundances (Kallman et al. 1996), our measured DR rate is a factor of $\sim 2 - 200$ times larger than these existing theoretical rates.

Also shown in Figure 4 is the recommended RR rate of Arnaud & Raymond (1992). Using existing theoretical DR rates, the total recombination rate (RR+DR) at $k_BT_e \sim 15$ eV barely exceeds the RR rate alone. Using our inferred DR rates yields a total recombination rate at $k_BT_e \sim 15$ eV which is a factor of ~ 1.5 larger than the RR rate alone.

For plasma modeling, we have fit our inferred Fe XVIII $\Delta n = 0$ Maxwellian-averaged DR rate coefficient to the simple fitting formula (Arnaud & Raymond 1992)

$$\alpha_{DR}(T_e) = T_e^{-3/2} \sum_i c_i e^{-E_i/k_BT_e}. \tag{6}$$

Here c_i and E_i are, respectively, the strength and energy parameters for the ith fitting component. Best fit values are listed in Table 6. The fit is good to better than 1.2% for $0.05 \leq k_BT_e \leq 10000$ eV. Below 0.05 eV, the fit goes to zero faster than our measured rate. This is unimportant as RR for $k_BT_e \leq 0.05$ eV is $\gtrsim 600$ times larger than DR.

Contributions due to DR into $n \geq n_{max} = 124$, which are not accessible in our setup are calculated theoretically to increase the DR rate by $\lesssim 2\%$. Hence, the zero density DR rate ($n_{max} = \infty$) is estimated to be $\lesssim 2\%$ larger than our inferred DR rate. Our calculations also show that DR into $n \geq 50(100)$ levels accounts for $\sim 20(10)\%$ of the total rate.

3.2.2. Fe XIX

The lowest energy, resolved DR resonance lies at 0.0660 ± 0.0005 eV. Below $E \sim 0.02$eV $\lesssim k_BT_\perp$, it is not possible to resolve resonances from the near 0 eV RR signal. We can, however, infer the presence of resonances below ~ 0.02 eV. The measured Fe XIX recombination rate at $\lesssim 10^{-3}$ eV is over a factor of ~ 10 larger than predicted using semiclassical RR theory with quantum mechanical corrections (Schippers et al. 1998). For Fe XVIII, this rate is only a factor of ~ 3 larger. A number of issues pertaining to RR measurements at collision energies $\lesssim 10^{-3}$ eV in electron coolers remain to be resolved (Hoffknecht et al. 1998; Schippers et al. 1998), but it is highly unlikely that their resolution will lead to RR rates that scale by a factor of ~ 3 for a change in ionic charge from 17 to 18. Thus, we infer that there are unresolved DR resonances contributing to the recombination signal below 0.02 eV. Our calculations suggest they are $2s^22p^4(^3P_1)20d$ resonances, but due to existing experimental and theoretical limitations, it is not possible unambiguously to identify these resonances.

We have used our measured resonance strengths and energies to calculate the Fe XIX to Fe XVIII $\Delta n = 0$ DR rate coefficient for an isotropic Maxwellian plasma. Our calculated rate is shown in Figure 5 for $k_BT_e \geq 0.2$ eV. Since the inferred, unresolved DR resonances below 0.02 eV are not included in our derived Maxwellian-averaged rate coefficient, the experimental DR rate should go to zero faster than the true DR rate. As it is extremely unlikely that Fe XIX will ever form at $k_BT_e \lesssim 0.2$ eV (Kallman et al. 1996), this uncertainty is expected to have an insignificant effect on plasma modeling. Above 0.2 eV we estimate the uncertainty in the absolute magnitude of our inferred rate to be less than 20%.

Existing theoretical Fe XIX $\Delta n = 0$ rate coefficients are also shown in Figure 5. For $T_e \lesssim 30$ eV the calculated rates of Roszman (1987b) and Dasgupta & Whitney (1994) both underestimate the DR rate, as does the Burgess formula (1965) using the oscillator strengths of Fuhr et al. (1988). All these calculations considered only DR via $2s - 2p$ core excitations and thus do not include DR via fine structure core excitations which, as shown by Savin et al. (1997), can be very important. Below $T_e \sim 30$ eV the rate of Dasgupta & Whitney goes to zero faster than that of Roszman. A partial explanation is that Dasgupta & Whitney do not account for DR into the $n = 6$ level.

The exact reason, however, is unclear. Roszman does not state the n level for which he calculates $2s-2p$ DR to be energetically allowed. This level may have been $n=6$; or if $n=7$, then the calculated resonance energies may be shifted by several or more eV below the true energies. For $T_e \gtrsim 30$ eV, both Roszman and Dasgupta & Whitney overestimate the DR rate. This may be partly due to their not accounting for autoionizations which leave the initial ion in a $2s^2 2p^4\ ^3P_0$ or $^3P_1$ state. At temperatures of ~ 70 eV, near where Fe XIX is predicted to form in photoionized gas of cosmic abundances (Kallman et al. 1996), Roszman overestimates the DR rate by a factor of ~ 1.5 and Dasgupta & Whitney by ~ 1.7, and the Burgess formula by ~ 1.1.

Also shown in Figure 5 is the recommended RR rate of Arnaud & Raymond (1992). At $k_B T_e \sim 70$ eV DR dominates over RR by a factor of ~ 2. Using the recommended RR rate and our inferred DR rate yields a total recombination rate ~ 1.4 smaller than that obtained using the published DR calculations of Roszman (1987b) or Dasgupta & Whitney (1994).

We have fit our inferred, Maxwellian-averaged DR rate coefficient using Equation 6. Best fit parameters are listed in Table 6. The fit reproduces our rate to better than 4% for $0.004 \leq k_B T_e \leq 10000$ eV. Below 0.004 eV, the fit goes to zero faster than our measured rate. However, for $k_B T_e \lesssim 0.2$ eV, the true rate is likely to be larger than either the fit or our inferred rate because of additional DR resonance contributions at $E \lesssim 0.02$ eV.

Contributions due to DR into $n \geq n_{max} = 130$, which are not accessible in our setup, are estimated to increase the DR rate by $\lesssim 4\%$. Hence, the zero density DR rate ($n_{max} = \infty$) is estimated theoretically to be $\lesssim 4\%$ larger than our inferred DR rate. Our calculations also show for Fe XIX that DR into $n \geq 50(100)$ levels accounts for $\sim 20(10)\%$ of the total rate.

4. New Theoretical Calculations

Accurate low temperature DR calculations are challenging both theoretically and computationally. Resonance energies often need to be known to better than $0.01-0.10$ eV, which for multi-electron ions can push theoretical techniques beyond their present capabilities (cf., DeWitt et al. 1996; Schippers et al. 1998) Also, approximations must be made to make the calculations tractable (Hahn 1993). To help benchmark current theoretical capabilities, we have carried out detailed state-of-the-art MCDF and multiconfiguration Breit Pauli (MCBP) calculations for comparison with our experimental results.

4.1. Multiconfiguration Dirac-Fock (MCDF) Method

DR resonance strengths and rate coefficients for Fe XVIII and Fe XIX are calculated in the independent processes and isolated resonance approximation (Seaton & Storey 1976). Required transition energies, Auger and radiative rates are evaluated using the MCDF method in intermediate coupling with configuration interaction within the same n complex (Chen 1985; Grant et al. 1980). All possible Coster-Kronig transitions and radiative transitions to bound states are included. For $2s + e^- \rightarrow 2pnl$ DR, a one-step cascade stabilization correction is taken into account when the intermediate state radiatively decays to another autoionizing state. All possible autoionization channels for the recombining ion are accounted for, including autoionization to an excited state of the initial ion.

For Fe XVIII, we include excitation from the ground state $1s^2 2s^2 2p^5\ ^2P_{3/2}$ to the $1s^2 2s^2 2p^5\ ^2P_{1/2}$ and $1s^2 2s 2p^6\ ^2S_{1/2}$ states. Explicit calculations are carried out for $18 \leq n \leq 36$ and $l \leq 8$ for $2p_{1/2} - 2p_{3/2}$ core excitations and for $6 \leq n \leq 36$ and $l \leq 8$ for $2s - 2p$ core excitations. Calculated excitation energies agree well with measurements (Corliss & Sugar 1982), and theoretical resonance energies are used without adjustment.

For Fe XIX, we include excitation from the ground state $1s^2 2s^2 2p^4\ ^3P_2$ to the $1s^2 2s^2 2p^4\ ^3P_0$, $^3P_1$, $^1D_2$, $^1S_0$ and the $1s^2 2s 2p^5\ ^3P^o_{0,1,2}$ and $^1P^o_1$ excited states. Using experimental core excitation energies (Corliss & Sugar 1982), the resonance energies are adjusted by $\lesssim 1$ eV for all levels except the $2s^2 2p^4 (^1S_0)$. The calculated energy of this level is 3.7 eV larger than its known value because the $2p^6 (^1S_0)$ state is not included in the configuration-interaction (CI) basis set. Had it been included, the calculated energy of the $2s^2 2p^4 (^1S_0)$ state would have decreased by ~ 3 eV. Its omission from the CI basis set has an insignificant effect on calculated autoionization rates. Explicit calculations are performed for $11 \leq n \leq 30$ and $l \leq 12$ for the fine-structure transitions (i.e., excitations to the first four excited states) and for $6 \leq n \leq 30$ and $l \leq 12$ for $2s - 2p$ excitations.

Extrapolation to higher n Rydberg states for both ions is done by using an n^{-3} scaling for the Auger and radiative rates. For Fe XVIII, extrapolations for $l > 8$ are calculated using a power law fitted to $l = 6$, 7, and 8. For Fe XIX, no high-l extrapolation is performed since by $l = 12$ the cross section has already converged to better than 1%.

4.2. Multiconfiguration Breit-Pauli (MCBP) Method

Again, the DR cross sections are calculated in the independent processes and isolated resonance approximations. Energy levels, autoionization and radiative rates are calculated in intermediate coupling using the multi-configuration code AUTOSTRUCTURE (Badnell 1986, 1997). All possible autoionizing transitions and radiative transitions to bound states are included. This includes autoionization of the recombining ion to all energetically allowed states of the initial ion. In addition, a one-step cascade is taken account of when the core electron of the intermediate state radiates and leaves the ion in an autoionizing state.

For Fe XVIII, explicit calculations are carried out for $6 \leq n \leq 124$ and $0 \leq l \leq 17$. For Fe XIX, explicit calculations are carried-out for $6 \leq n \leq 130$ and $0 \leq l \leq 15$. Configuration mixing within and between n manifolds is taken into account between all recombined and recombining configurations with $n \leq 6$. For $n \geq 7$, configuration mixing is restricted to the core only. Rydberg–Rydberg radiative transitions $n \to n'$ were calculated hydrogenically for $n' \geq 7$. The calculated core energies for Fe XVIII and FeXIX were adjusted by $\lesssim 0.6$ eV to match the observed values (Kelly 1987). This gives a marked improvement to resonance positions, which in general are not known *a priori*.

4.3. Comparison with Experiment

Tables 2 and 3 list the new theoretical resonance energies and strengths for Fe XVIII DR via the ${}^2P_{3/2} - {}^2P_{1/2}$ and ${}^2P_{3/2} - {}^2S_{1/2}$ core excitations, respectively. The new theoretical resonance strengths and energies for Fe XIX are listed in Table 4.

In Figures 6 and 7 we plot for the Fe XVIII ${}^2P_{3/2} - {}^2P_{1/2}$ and ${}^2P_{3/2} - {}^2S_{1/2}$ channels, respectively, the experimental and theoretical values of $\hat{\sigma}_n E_n = E_{nl(l \gtrsim 3)} \sum_l \hat{\sigma}_{nl}$. We have multiplied $\hat{\sigma}_n$ by E_n to remove the trivial energy dependence on the right-hand-side of Equation 2. There is an $\sim 20\%$ to $\sim 40\%$ discrepancy for the entire ${}^2P_{3/2} - {}^2P_{1/2}$ series. This increases with n and reaches a value of $\sim 50\%$ for the summed series limit. These differences are larger than the total experimental uncertainty. For the ${}^2P_{3/2} - {}^2S_{1/2}$ series (Figure 7), there is an $\sim 10 - 18\%$ difference. Also clearly visible is the opening up of the $2s2p^6({}^2S_{1/2})nl \to 2s^22p^5({}^2P_{1/2}) + e^-$ autoionization channel near $E = 119$ eV, which causes an abrupt decrease in $\hat{\sigma}_n E_n$ between $n = 17$ and 18. This channel was also observed by Lampert et al. (1996) for the isoelectronic ion Se XXVI.

In Figures 8 to 11 we plot $\hat{\sigma}_n E_n$ using $E_{nl(l \gtrsim 4)}$ for the Fe XIX ${}^3P_2 - {}^3P_1$, ${}^3P_2 - {}^1D_2$, ${}^3P_2 - {}^3P_2^o$ and ${}^3P_2 - {}^3P_1^o$ DR channels, respectively. For the ${}^3P_2 - {}^3P_1$ and ${}^3P_2 - {}^1D_2$ series, we include measured values for only those resonances which are unambiguously resolved in our experiment from surrounding resonances. For example, for the ${}^3P_2 - {}^3P_1$ series, we do not plot the experimental values for $\hat{\sigma}_{29} E_{29}$ because the $2s^22p^4({}^3P_1)29l$ resonance is a weak feature on the shoulder of the strong $2s^22p^4({}^1D_2)17l$ $(l \geq 2)$ resonance. However, for the ${}^3P_2 - {}^1D_2$ series we do plot $\hat{\sigma}_{17} E_{17}$ because any blending from the $2s^22p^4({}^3P_1)29l$ resonance is expected to introduce only a small error. For this series we also do not plot the measured value of $\hat{\sigma}_{21} E_{21}$. It blends with the ${}^3P_2 - {}^3P_1$ series limit. For the ${}^3P_2 - {}^3P_2^o$ and ${}^3P_2 - {}^3P_1^o$ series, we use theory to subtract out the different $2s2p^5({}^1P_1^o)6l$ resonance strengths from the various $n = 7$ resonances. This is estimated to introduce a negligible error. The $2s2p^5({}^3P_2^o)14p$ and $2s2p^5({}^3P_1^o)12l$ $(l \geq 2)$ blend is resolved using the theoretical resonance strength for the $14p$ resonance. In general, agreement between experiment and theory is good, with a few exceptions such as the MCDF resonance strength for the $2s^22p^4({}^3P_0)22l$ $(l \geq 3)$ resonance and the MCBP resonance strength for the $2s2p^5({}^3P_1^o)7f$ resonance. The reason for the discrepancies between theory and experiment for these resonances as well as for the summed resonance strengths of the ${}^3P_2 - {}^3P_2^o$ and ${}^3P_2 - {}^3P_1^o$ series limits is not understood.

The Maxwellian-averaged rate coefficients from our new Fe XVIII and Fe XIX MCDF DR calculations are plotted in Figures 4 and 5. The theoretical rates agree with our inferred rates to within $\sim 30\%$. Though not shown, the MCBP rates agrees well with the MCDF calculations. We have fit our MCDF rates using Equation 6. Note that for Fe XIX we do not include the near 0 eV $2s^2 2p^4[^3P_1]20d$ resonances. Best fit values are listed in Table 6. For Fe XVIII, the fit is good to better than 2% for $0.06 \leq k_B T_e \leq 10000$ eV. Below 0.06 eV, the fit goes to zero faster than theory. For Fe XIX, the fit is good to better than 2% for $0.001 \leq k_B T_e \leq 10000$ eV.

5. Astrophysical Implications for Photoionized Gas

5.1. Ionization Balance Calculations

Cosmic plasmas are most commonly modeled using the compiled DR rates of Aldrovandi & Péquignot (1973), Shull & van Steenberg (1982), Arnaud & Rothenflug (1985), and Arnaud & Raymond (1992). For photoionized gases the rates of Nussbaumer & Storey (1983) are often used. And recently Nahar & Pradhan (1994; 1995) and Nahar (1997) have calculated the unified electron-ion recombination rates (e.g., RR+DR) for a number of ions. But for a few exceptions, these rates have all been calculated either using LS-coupling without accounting for $nlj \rightarrow nlj'$ fine-structure transitions or using the Burgess formula (Burgess 1965), which neither takes these fine structure transitions into account nor can account for core excitations not connected to the ground state via an electric dipole transition.

Our results demonstrate that the Burgess formula, LS-coupling, intermediate coupling, and even MCDF calculations can easily under- or over-estimate the Maxwellian-averaged $\Delta n = 0$ DR rate by factors of ~ 2 at "high" T_e or underestimate it by factors of ~ 2 to orders of magnitude at "low" T_e. The limit between "low" and "high" temperature here is given roughly by the comparison of $k_B T_e$ with the fine-structure core excitation energy ΔE_{fs}, typically 10-20 eV for the iron L shell ions. Our results also demonstrate that a detailed comparison between theory and experiment of the resonance strengths and energies that go into the total rate coefficient is the only way to distinguish unambiguously between different theoretical rate coefficients.

The importance at some $k_B T_e$ of a given DR channel can be estimated using Equation 1. For an ion with fine-structure (i.e. an ion with a partially filled p, d, etc., shell), DR via fine-structure core excitations usually dominates the DR process if the ion forms at $k_B T_e \lesssim \Delta E_{fs}$. Nearly all existing calculations do not account for this channel, and hence they almost certainly underestimate the $\Delta n = 0$ DR rate by factors of ~ 2 to orders of magnitude. For ions which form at $k_B T_e \gtrsim \Delta E_{fs}$, fine-structure core excitations are no longer important and DR is dominated by $nlj \rightarrow nl'j'$ $(l \neq l')$ channels. Our measurements demonstrate that DR calculations via these other $\Delta n = 0$ channels can readily under- or over-estimate the DR rate by factors of ~ 2. Taken together, our results call into question all existing theoretical $\Delta n = 0$ DR rates used for ionization balance calculations of cosmic plasmas.

5.2. Thermal Instability

Hess, Kahn, & Liedahl (1997) showed that Fe L ions play an important role in determining the range in parameter space over which photoionized gas is predicted to be thermally unstable. But they found the existence of the instability was robust to changes in elemental abundance and the shape of the ionizing spectrum. Reynolds & Fabian (1995) found the instability was robust to changes in density, optical depth, and the shape of the ionizing spectrum. Hess et al. also studied the effects of new Fe L $\Delta n = 0$ DR rates published after the compilation of Arnaud & Rothenflug (1992) and found no significant effects.

Our measurements, which demonstrate that published Fe L $\Delta n = 0$ DR rates can be wrong by factors of ~ 2 or more, call into question this last conclusion of Hess et al. (1997). We have used XSTAR (version 1.40b; Kallman & Krolik 1997) to re-investigate the effects on the thermal instability of photoionized gas due to our estimated factor of 2 errors in the Fe XX through Fe XXIV $\Delta n = 0$ DR rates. For Fe XVIII and Fe XIX, we use our inferred DR rates. Because the DR rates in XSTAR do not account for DR via fine-structure core excitations, we have used the Fe XVIII and Fe XIX results to estimate the DR rates via $2p_{1/2} \rightarrow 2p_{3/2}$ core excitations for Fe XX through Fe XXII. We have run XSTAR using Fe XX through Fe XXIV $\Delta n = 0$ DR rates unchanged, increased by a factor of two, and decreased by the same factor. We assume cosmic abundances; and similar to Reynolds & Fabian (1995), we assume a model AGN ionizing continuum consisting of a photon number power law $N \propto E^{-1.8}$ which extends from 13.6 eV to 40 keV. Here E is the photon energy.

Figure 12 shows the predicted T_e versus the ionization parameter $\xi = L/n_H r^2$, where L is the luminosity of the ionizing source, n_H is the hydrogen nucleus density, and r is the distance from the ionizing source. Figure 13 is a phase diagram of the gas. For the different DR rates, T_e is shown for steady-state condition (where heating and cooling of the gas are equal) versus $\xi/T_e \propto F/p$. Here F is the ionizing flux and p is the pressure of the gas. The well-known thermal instability of photoionized gas in steady-state can be seen for $-3.80 \lesssim \log(\xi/T_e) \lesssim -3.35$, where ξ is in units of ergs cm s^{-1} and T_e in K.

The estimated uncertainty in the DR rates results in as much as a factor of ~ 1.8 difference between predicted values of T_e. And should a future observation yield $\log T_e \sim 6.1$ (where T_e is in K), then the uncertainty in the inferred ξ would be a factor of ~ 3.4. Astrophysically, for observations in this range of ξ, these uncertainties will hamper our ability to determine L or n_e to within a factor of ~ 3.4 or r to within a factor of ~ 1.8. Also, while the uncertainties in the DR rates do not remove the thermal instability, they do dramatically affect the range in parameter space over which the instability is predicted to exist. The range changes by a factor of ~ 1.8 in ξ/T_e and a factor of ~ 2.2 in T_e. When we have completed our measurements for all the Fe L $\Delta n = 0$ DR rates, we will be able to resolve this problem formally.

The above results demonstrate the effects of the uncertainties in the DR rates for Fe L ions. Calculated rates for other ions are likely to have similar errors. In order to model photoionized gases accurately, corrections to the DR rates for all the relevant ions will be required. However, the ionization structure of photoionized gas is not a simple function of temperature. The temperature at which an ion forms depends upon the shape of the ionizing spectrum, the metallicity of the gas, additional heating and cooling mechanisms, and radiative transfer effects. An ion forming at a given T_e in one object could potentially form at a different T_e in another. Because it is unknown *a priori* what T_e of the observed gas will be, it is important to use DR rates with the correct T_e dependence over the entire T_e range of interest.

5.3. Line Emission

In photoionized gases, lines produced by $\Delta n = 0$ DR provide the basis for new classes of electron temperature and density diagnostics (Liedahl 1992; Kahn & Liedahl 1995; Savin et al. 1998). DR is a resonance process and has a T_e dependence different from RR. Thus, ratios of DR and RR produced lines can be used as a T_e diagnostic.

One class of T_e diagnostics is based on $2s + e^- \rightarrow 2pnl$ DR (see Liedahl 1992 for an extensive discussion; also Kahn & Liedahl 1995). For low n values, the recombining ion can radiatively stabilize by a decay of the captured electron. This occurs in the presence of an excited core. The resulting lines are spectroscopically distinct from those produced by RR.

Another class of T_e and n_e diagnostics involves DR via fine-structure core excitations (Savin et al. 1998). The excited core cannot decay via an electric dipole transition and the ion stabilizes by a radiative decay of the captured electron, which is typically in a high n level (here, $n \gtrsim 15$). This leads to an enhancement of $n \rightarrow 3$ line emission which will appear as broad transition arrays at *AXAF* and *XMM* resolution. Their widths offer a possible n_e diagnostic. As n_e increases, the highest n level which radiatively stabilizes before it is collisionally ionized decreases. This reduces the maximum energy of the photons in the transition array and results in a decrease in the width of the spectral feature.

A detailed discussion of these various diagnostics will be the topic of a future paper (Liedahl et al., in preparation). Further experimental work is under way to benchmark the DR calculations necessary to develop these diagnostics.

The authors thank T. R. Kallman and S. T. Manson for helpful discussions. This work was supported in part by NASA High Energy Astrophysics X-Ray Astronomy Research and Analysis grant NAG5-5123. Travel and living expenses for D.W.S. were supported by NATO Collaborative Research Grant CRG-950911. The experimental work has been supported in part by the German Federal Minister for Education, Science, Research, and Technology (BMBF) under Contract Nos. 06 GI 475, 06 GI 848, and 06 HD 854I. Work performed at Lawrence Livermore National Laboratory was under the auspices of the US Department of Energy (contract number W-7405-ENG-48).

Table 1. Energy levels (relative to the ground state) for the $n = 2$ shells of Fe XVIII and Fe XIX (Sugar & Corliss 1985)

Ion	Level	Energy (eV)
Fe^{17+}	$2s^22p^5\ ^2P_{3/2}$	0
	$2s^22p^5\ ^2P_{1/2}$	12.7182
	$2s2p^6\ ^2S_{1/2}$	132.0063
Fe^{18+}	$2s^22p^4\ ^3P_2$	0
	$2s^22p^4\ ^3P_0$	9.3298
	$2s^22p^4\ ^3P_1$	11.0893
	$2s^22p^4\ ^1D_2$	20.9350
	$2s^22p^4\ ^1S_0$	40.3122
	$2s2p^5\ ^3P_2^o$	114.4238
	$2s2p^5\ ^3P_1^o$	122.0922
	$2s2p^5\ ^3P_0^o$	127.7063
	$2s2p^5\ ^1P_1^o$	157.1624
	$2p^6\ ^1S_0$	264.6047

Table 2. Comparison of the measured and calculated Fe XVIII to Fe XVII $\Delta n = 0$ DR resonance energies E_{nl} and energy-integrated cross sections $\hat{\sigma}_{nl}$ for the $2s^2 2p^5 (^2P_{1/2}) nl$ resonances.

	E_d (eV)			$\hat{\sigma}_d$ (10^{-21} cm^2 eV)		
nl	MCDF[a]	MCBP[a]	Experiment[b,c]	MCDF	MCBP	Experiment[b]
$18s$	0.1730	0.1981	0.2008 ± 0.0007	148.5	119.8	156.7 ± 10.1
$18p$	0.3087	0.3312	0.3373 ± 0.0007	200.9	253.7	278.6 ± 9.1
$18d$	0.4683	0.4908	0.4983 ± 0.0007	473.7	529.1	591.6 ± 8.1
$18l$ ($l \geq 3$)	0.5477	0.5702	0.5818 ± 0.0003	1083.7	1105.4	1425.9 ± 9.3
$n = 18$ (sum)				1906.8	2008.4	2452.8 ± 18.3
$19s$	1.475	1.499	1.494 ± 0.008	13.1	13.5	18.6 ± 5.2
$19p$	1.590	1.612	1.621 ± 0.003	36.6	44.9	52.8 ± 5.9
$19d$	1.725	1.748	1.760 ± 0.002	109.9	127.4	139.5 ± 7.7
$19l$ ($l \geq 3$)	1.793	1.815	1.831 ± 0.002	290.1	291.8	394.8 ± 7.8
$n = 19$ (sum)				449.7	477.6	605.7 ± 13.5
$20s$	2.583	2.607	2.631 ± 0.015	6.4	6.6	9.7 ± 2.7
$20p$	2.682	2.704	2.728 ± 0.008	18.6	22.9	28.9 ± 3.9
$20d$	2.798	2.820	2.839 ± 0.004	58.3	67.6	61.6 ± 5.9
$20l$ ($l \geq 3$)	2.855	2.878	2.898 ± 0.001	156.4	155.1	236.3 ± 6.2
$n = 20$ (sum)				239.7	252.2	336.5 ± 8.6
$21s$	3.535	3.569	3.572 ± 0.022	4.0	3.6	9.7 ± 3.9
$21p$	3.620	3.649	3.666 ± 0.020	11.8	13.2	11.6 ± 3.9
$21l$ ($l \geq 2$)	3.756	3.792	3.802 ± 0.001	138.7	144.3	184.1 ± 4.1
$n = 21$ (sum)				154.5	161.1	205.4 ± 6.9
$22l$ ($l \geq 0$)	4.536	4.560	4.591 ± 0.002	111.1	113.2	140.7 ± 4.2
$23l$ ($l \geq 0$)	5.231	5.254	5.281 ± 0.002	84.4	83.9	111.7 ± 4.0
$24l$ ($l \geq 0$)	5.841	5.864	5.890 ± 0.002	66.7	66.0	87.3 ± 2.8
$25l$ ($l \geq 0$)	6.379	6.401	6.427 ± 0.003	53.9	52.9	76.7 ± 2.7
$26l$ ($l \geq 0$)	6.856	6.878	6.902 ± 0.003	44.8	43.7	66.2 ± 2.8
$27l$ ($l \geq 0$)	7.281	7.303	7.324 ± 0.004	37.4	36.7	56.5 ± 2.8
$28l$ ($l \geq 0$)	7.661	7.683	7.696 ± 0.004	31.9	31.3	46.3 ± 2.8
$29l$ ($l \geq 0$)	8.002	8.024	8.031 ± 0.004	27.7	27.0	43.3 ± 2.2
$30l$ ($l \geq 0$)	8.310	8.332	8.349 ± 0.005	24.1	23.5	35.6 ± 2.2
$31l$ ($l \geq 0$)	8.589	8.611	8.624 ± 0.005	21.1	20.7	34.9 ± 2.2
$32l$ ($l \geq 0$)	8.841	8.852	8.862 ± 0.006	18.7	18.4	31.9 ± 2.2
$33l \leq n \lesssim 124l$ ($l \geq 0$)			$8.94 - 12.72$	218.0	222.7	340.6 ± 14.5

[a] Resonance strength weighted energy: $E_d = \sum_i E_i \sigma_i / \sum_i \sigma_i$.

[b] 1σ statistical fitting uncertainties only.

[c] Absolute energy scale uncertainty $\lesssim 0.4\%$.

Table 3. Comparison of the measured and calculated Fe XVIII to Fe XVII $\Delta n = 0$ DR resonance energies E_{nl} and energy-integrated cross sections $\hat{\sigma}_{nl}$ for the $2s2p^6(^2S_{1/2})nl$ resonances.

	E_d (eV)			$\hat{\sigma}_d$ (10^{-21} cm^2 eV)		
nl	MCDF[a]	MCBP[a]	Experiment[b,c]	MCDF	MCBP	Experiment[b]
$6s$ $(J = 1)$	12.107	11.955	11.879 ± 0.005	54.2	51.6	55.7 ± 3.4
$6s$ $(J = 0)$	12.685	12.503	12.374 ± 0.011	15.6	16.1	25.8 ± 2.9
$6p_{1/2}$ $(J = 0, 1)$	15.909	15.715	15.599 ± 0.010	27.3	27.9	30.7 ± 4.7
$6p_{3/2}$ $(J = 1, 2)$	16.238	16.039	15.917 ± 0.008	72.1	78.8	109.2 ± 6.3
$6d_{3/2}$ $(J = 1, 2)$, $6d_{5/2}$ $(J = 3)$	20.520	20.332	20.203 ± 0.003	133.1	132.1	144.7 ± 4.0
$6d_{5/2}$ $(J = 2)$	21.000	20.851	20.678 ± 0.007	39.6	41.8	49.5 ± 3.8
$6f$	22.693	22.542	22.395 ± 0.002	260.2	272.3	299.0 ± 7.1
$6l$ $(l \geq 4)$	22.950	22.798	22.709 ± 0.001	408.3	411.9	525.6 ± 7.3
$n = 6$ (sum)				1010.3	1032.5	1240.2 ± 14.8
$7s$	45.282	45.172	$44.789 - 45.938$[d]	9.3	12.3	21.8 ± 4.7
$7p$	47.702	47.533	47.438 ± 0.017	23.6	35.2	38.0 ± 3.7
$7d$	50.474	50.309	50.175 ± 0.011	53.2	60.8	62.2 ± 3.6
$7l$ $(l \geq 3)$	51.882	51.683	51.647 ± 0.003	249.6	271.8	290.0 ± 4.1
$n = 7$ (sum)				335.7	380.1	412.0 ± 8.1
$8s$	66.332	66.186	$65.761 - 66.410$[d]	5.3	6.0	4.1 ± 3.0
$8p$	67.934	67.751	67.688 ± 0.032	13.3	18.1	12.6 ± 3.1
$8d$	69.769	69.588	69.522 ± 0.022	31.2	33.5	29.3 ± 3.2
$8l$ $(l \geq 3)$	70.722	70.526	70.515 ± 0.003	185.8	189.4	207.9 ± 3.3
$n = 8$ (sum)				235.6	247.0	253.9 ± 5.5
$9p$	81.681	81.493	81.422 ± 0.027	9.5	12.4	7.1 ± 1.7
$9d$	82.959	82.772	82.675 ± 0.019	22.4	23.3	22.8 ± 2.3
$9l$ $(l \geq 3)$	83.631	83.437	83.404 ± 0.003	155.7	156.0	173.1 ± 2.7
$n = 9$ $(l \geq 1$ sum)				187.6	191.6	203.0 ± 3.9
$10p$	91.445	91.256	$90.876 - 91.476$[d]	7.7	9.6	5.5 ± 2.3
$10l$ $(l \geq 2)$	92.808	92.612	92.620 ± 0.005	160.2	155.6	160.6 ± 4.0
$n = 10$ $(l \geq 1$ sum)				167.9	165.2	166.1 ± 4.6
$11l$ $(l \geq 2)$	99.651	99.459	99.418 ± 0.007	148.6	140.0	153.1 ± 3.9
$12l$ $(l \geq 2)$	104.855	104.663	104.658 ± 0.007	138.8	128.6	134.0 ± 3.9
$13l$ $(l \geq 2)$	108.903	108.711	108.701 ± 0.007	130.1	119.6	128.1 ± 3.6
$14l$ $(l \geq 1)$	112.094	111.898	111.925 ± 0.005	127.3	118.0	120.8 ± 2.4
$15l$ $(l \geq 1)$	114.678	114.493	114.525 ± 0.007	119.7	111.3	113.8 ± 2.4
$16l$ $(l \geq 0)$	116.800	116.608	116.618 ± 0.007	114.5	107.2	112.0 ± 2.4
$17l$ $(l \geq 0)$	118.561	118.368	118.374 ± 0.007	108.2	101.8	105.5 ± 2.4
$18l$ $(l \geq 0)$	120.038	119.844	119.846 ± 0.009	87.1	82.4	84.1 ± 2.5
$19l$ $(l \geq 0)$	121.285	121.092	121.075 ± 0.009	82.3	78.0	86.5 ± 2.5

Table 3. Continued.

	E_d (eV)			$\hat{\sigma}_d$ (10^{-21} cm^2 eV)		
nl	MCDF[a]	MCBP[a]	Experiment[b,c]	MCDF	MCBP	Experiment[b]
$20l$ ($l \geq 0$)	122.350	122.157	122.130 ± 0.010	77.9	74.1	81.1 ± 2.5
$21l$ ($l \geq 0$)	123.267	123.074	123.051 ± 0.012	74.1	70.8	73.1 ± 2.5
$22l$ ($l \geq 0$)	124.061	123.869	123.872 ± 0.013	70.4	67.5	76.4 ± 2.5
$23l$ ($l \geq 0$)	124.754	124.562	124.577 ± 0.017	67.0	64.4	72.7 ± 2.8
$24l \leq n \lesssim 124l$ ($l \geq 0$)			$125.0 - 132.5$	1575.9	1552.3	1532.1 ± 8.9

[a] Resonance strength weighted energy: $E_d = \sum_i E_i \sigma_i / \sum_i \sigma_i$.

[b] 1σ statistical fitting uncertainties only.

[c] Absolute energy scale uncertainty $\lesssim 0.4\%$.

[d] Unable to fit for resonance energy.

Table 4. Comparison of the measured and calculated resonance energies E_d and energy-integrated DR cross sections $\hat{\sigma}_d$ of Fe XIX to Fe XVIII $\Delta n = 0$ DR.

	E_d (eV)			$\hat{\sigma}_d$ (10^{-21} cm^2 eV)		
Resonance	MCDF[a]	MCBP[a]	Experiment[b,c]	MCDF	MCBP	Experiment[b]
$2s^22p^4(^3P_1)20l\ (l \geq 3)$	0.0619	0.0623		6218.7	7375.5	
$2s^22p^4(^3P_0)22p$	0.0993	0.0970		186.8	226.3	
blend	0.0628	0.0633	0.0660 ± 0.0005	6405.5	7601.8	6726.2 ± 180.2
$2s^22p^4(^3P_0)22d$	0.1792	0.1754	0.1824 ± 0.0007	391.0	455.0	360.4 ± 15.1
$2s^22p^4(^3P_0)22l\ (l \geq 3)$	0.2236	0.2204	0.2294 ± 0.0004	770.1	658.2	538.4 ± 9.3
$2s^22p^4(^1D_2)15s$	0.7064	0.7103	0.7054 ± 0.0062	126.5	140.1	110.5 ± 7.0
$2s^22p^4(^1D_2)15p$	0.9410	0.9450		260.3	305.1	
$2s^22p^4(^3P_1)21p$	0.9421	0.9456		68.8	85.6	
$2s^22p^4(^3P_0)23d$	0.9601	0.9562		64.1	73.1	
blend	0.9444	0.9469	0.9545 ± 0.0012	393.2	463.8	429.9 ± 7.3
$2s^22p^4(^3P_1)21l\ (l \geq 2)$	1.0677	1.0657	1.0780 ± 0.0017	661.6	587.8	487.3 ± 7.1
$2s^22p^4(^1D_2)15d$	1.2017	1.1999	1.2052 ± 0.0003	832.4	928.4	746.1 ± 4.8
$2s^22p^4(^1D_2)15l\ (l \geq 3)$	1.3323	1.3299	1.3366 ± 0.0003	1067.8	1028.1	871.5 ± 4.7
$2s^22p^4(^3P_0)24l\ (l \geq 1)$	1.6598	1.6552	1.6812 ± 0.0054	114.6	108.9	99.4 ± 4.8
$2s^22p^4(^3P_1)22p$	1.8502	1.8585	1.8282 ± 0.0157	30.4	37.0	22.5 ± 7.1
$2s^22p^4(^3P_1)22l\ (l \geq 2)$	1.9592	1.9584	1.9783 ± 0.0050	316.9	292.3	261.1 ± 7.9
$2s^22p^4(^3P_0)25l\ (l \geq 0)$	2.2627	2.2568	2.2877 ± 0.0062	82.4	74.7	74.0 ± 5.2
$2s^22p^4(^3P_1)23l\ (l \geq 0)$	2.7235	2.7102		224.1	218.9	
$2s^22p^4(^3P_0)26l\ (l \geq 0)$	2.7971	2.7940		59.5	63.9	
$2s^22p^4(^1S_0)11p$	2.8421	2.8374		47.7	50.4	
$2s2p^5(^3P^o_0)6d\ (J = 5/2)$	2.8788	2.9405		73.2	75.0	
blend	2.7764	2.7813	2.7888 ± 0.0083	404.5	408.2	367.2 ± 12.9
$2s2p^5(^3P^o_0)6d\ (J = 3/2)$	3.0216	3.0655	2.9699 ± 0.0233	42.2	27.7	44.7 ± 11.4
$2s^22p^4(^1D_2)16l\ (l \leq 1)$	3.3315	3.3797		83.2	95.1	
$2s^22p^4(^3P_1)24l\ (l \geq 0)$	3.4072	3.4072		157.6	157.5	
$2s^22p^4(^1S_0)11d$	3.4983	3.4992		154.4	163.8	
blend	3.4267	3.4292	3.4852 ± 0.0030	395.2	416.4	298.3 ± 7.7
$2s^22p^4(^1D_2)16l\ (l \geq 2)$	3.6627	3.6560		556.8	556.6	
$2s^22p^4(^1S_0)11f$	3.8198	3.8179		42.2	26.9	
blend	3.6739	3.6635	3.7175 ± 0.0019	599.0	583.5	574.2 ± 8.9

Table 4. Continued.

	E_d (eV)			$\hat{\sigma}_d$ (10^{-21} cm^2 eV)		
Resonance	MCDF[a]	MCBP[a]	Experiment[b,c]	MCDF	MCBP	Experiment[b]
$2s^22p^4(^1S_0)11l$ $(l \geq 4)$	3.8731	3.8727		17.4	24.4	
$2s^22p^4(^3P_1)25l$ $(l \geq 0)$	4.0102	4.0123		116.3	116.1	
$2s^22p^4(^3P_0)29l$ $(l \geq 0)$	4.0814	4.0768		28.4	27.5	
blend	4.0086	4.0025	4.0717 ± 0.0006	162.1	168.0	159.9 ± 2.8
$2s^22p^4(^3P_1)26l$ $(l \geq 0)$	4.5449	4.5455	4.5791 ± 0.0145	92.6	96.9	101.0 ± 7.9
$2s2p^5(^3P^o_0)6f$	4.8966	4.9530		50.0	50.8	
$2s^22p^4(^3P_1)27l$ $(l \geq 0)$	5.0212	5.0273		74.7	80.5	
blend	4.9701	4.9986	5.0714 ± 0.0107	124.7	131.3	121.2 ± 12.9
$2s^22p^4(^3P_1)28l$ $(l \geq 0)$	5.4473	5.4508	5.4803 ± 0.0127	61.7	61.2	56.3 ± 9.3
$2s^22p^4(^1D_2)17l$ $(l \geq 2)$	5.6385	5.6326	5.6779 ± 0.0035	296.0	299.8	297.1 ± 8.6
$2s^22p^4(^3P_1)29l$ $(l \geq 0)$	5.8299	5.8331	5.8797 ± 0.0095	50.9	50.6	83.8 ± 6.1
$2s^22p^4(^3P_1)30l$ $(l \geq 0)$	6.1750	6.1780	6.2025 ± 0.0149	44.2	42.9	52.9 ± 3.4
$2s^22p^4(^3P_1)31l$ $(l \geq 0)$	6.4987	6.4903	6.5297 ± 0.0187	37.5	37.0	49.1 ± 4.0
$2s^22p^4(^3P_1)32l$ $(l \geq 0)$	6.7809	6.7721	6.7801 ± 0.0241	32.6	32.5	41.7 ± 6.2
$2s^22p^4(^3P_1)33l$ $(l \geq 0)$	7.0378	7.0313		28.7	28.3	
$2s^22p^4(^1D_2)18l$ $(l \leq 1)$	7.0628	7.0640		28.2	31.4	
blend	7.0502	7.0485	7.0426 ± 0.0181	56.9	59.7	53.0 ± 6.2
$2s^22p^4(^1D_2)18l$ $(l \geq 2)$	7.2941	7.2884	7.2885 ± 0.0029	196.3	194.2	143.5 ± 10.0
$2s^22p^4(^1D_2)19l$ $(l \geq 1)$	8.6945	8.6723	8.7245 ± 0.0056	138.0	154.3	142.5 ± 3.4
$2s^22p^4(^1S_0)12p$	8.9022	8.9037	8.9874 ± 0.0249	11.9	14.8	14.3 ± 2.7
$2s^22p^4(^1S_0)12d$	9.4051	9.4051	9.4507 ± 0.0138	44.4	34.9	27.6 ± 3.1
$2s^22p^4(^1S_0)12l$ $(l \geq 3)$	9.6654	9.6651		18.3	11.6	
$2s^22p^4(^1D_2)20l$ $(l \geq 0)$	9.8697	9.8647		118.5	106.2	
blend	9.8424	9.8450	9.9320 ± 0.0066	136.8	117.8	97.2 ± 3.8
$2s^22p^4(^1D_2)21l$ $(l \geq 0)$	10.903	10.896	10.951 ± 0.008	83.4	82.8	66.5 ± 3.3
$2s^22p^4(^3P_1)nl$ $(34 \leq n \lesssim 130,\ l \geq 0)$			$7.1 - 11.7$	422.2	325.0	379.6 ± 16.5
$2s^22p^4(^1D_2)22l$ $(l \geq 0)$	11.800	11.794	11.814 ± 0.005	55.4	54.0	51.6 ± 2.1
$2s^22p^4(^1D_2)23l$ $(l \geq 0)$	12.579	12.573	12.600 ± 0.007	44.9	44.2	37.5 ± 2.1
$2s^22p^4(^1D_2)24l$ $(l \geq 0)$	13.262	13.258	13.299 ± 0.008	38.0	36.5	34.5 ± 2.1

Table 4. Continued.

	E_d (eV)			$\hat{\sigma}_d$ (10^{-21} cm^2 eV)		
Resonance	MCDF[a]	MCBP[a]	Experiment[b,c]	MCDF	MCBP	Experiment[b]
$2s^22p^4(^1D_2)25l$ $(l \geq 0)$	13.865	13.862		31.4	30.3	
$2s^22p^4(^1S_0)13d$	13.994	13.993		10.1	10.3	
blend	13.897	13.895	13.903 ± 0.009	41.5	40.6	36.5 ± 2.2
$2s^22p^4(^1S_0)13l$ $(l \geq 3)$	14.205	14.203		7.6	4.6	
$2s^22p^4(^1D_2)26l$ $(l \geq 0)$	14.400	14.397		26.9	25.7	
blend	14.349	14.368	14.398 ± 0.011	34.5	30.3	32.0 ± 2.5
$2s^22p^4(^1D_2)27l$ $(l \geq 0)$	14.876	14.873	14.892 ± 0.016	23.2	22.2	22.8 ± 2.5
$2s^22p^4(^1D_2)28l$ $(l \geq 0)$	15.302	15.299	15.288 ± 0.021	20.2	19.3	17.5 ± 2.4
$2s^22p^4(^1D_2)29l$ $(l \geq 0)$	15.684	15.682	15.704 ± 0.024	17.7	17.0	15.9 ± 2.4
$2s2p^5(^3P^o_2)7s$ $(J = 5/2)$	17.890	17.943	17.912 ± 0.066	22.6	21.1	27.2 ± 2.4
$2s2p^5(^3P^o_2)7s$ $(J = 3/2)$	18.220	18.270	18.263 ± 0.065	12.7	11.9	15.5 ± 2.4
$2s2p^5(^3P^o_2)7p_{1/2}$ $(J = 3/2, 5/2)$	20.211	20.253	20.320 ± 0.017	43.2	43.4	46.1 ± 4.4
$2s2p^5(^3P^o_2)7p_{3/2}$ $(J = 3/2, 5/2, 7/2)$	20.466	20.494	20.566 ± 0.008	106.2	114.1	110.5 ± 7.0
$2s^22p^4(^1D_2)nl$ $(30 \leq n \lesssim 130,\ l \geq 0)$			$15.8 - 21.0$	204.4	198.6	208.7 ± 12.8
$2s2p^5(^3P^o_2)7d_{5/2}$ $(J = 9/2)$	22.785			36.5		
$2s2p^5(^3P^o_2)7d_{3/2}$ $(J = 3/2, 5/2, 7/2)$	22.857			81.0		
blend	22.830	22.859	22.828 ± 0.011	117.5	108.4	109.0 ± 4.1
$2s2p^5(^3P^o_2)7d_{5/2}$ $(J = 5/2, 7/2)$	23.127	23.156	23.144 ± 0.015	54.6	51.3	63.7 ± 3.3
$2s2p^5(^3P^o_2)7d_{5/2}$ $(J = 1/2, 3/2)$	23.439	23.497	23.460 ± 0.016	53.9	63.4	44.6 ± 3.3
$2s2p^5(^3P^o_2)7f$	24.224	24.260	24.223 ± 0.015	267.8	295.4	238.1 ± 7.2
$2s2p^5(^3P^o_2)7l$ $(l \geq 4)$	24.410	24.444		500.0	664.0	
$2s2p^5(^1P^o_1)6s$	24.413	24.471		6.8	6.3	
blend	24.410	24.444	24.458 ± 0.015	506.8	670.3	633.1 ± 8.3
$2s2p^5(^3P^o_1)7p$	28.082	28.060		42.9	45.5	
$2s2p^5(^1P^o_1)6p$	28.293	28.293		12.1	13.1	
blend	28.142	28.112	28.082 ± 0.012	55.0	58.6	47.0 ± 3.4
$2s2p^5(^3P^o_1)7d$	30.649	30.728	30.651 ± 0.010	56.7	75.4	67.5 ± 3.5
$2s2p^5(^3P^o_1)7f$	31.899	31.925	31.901 ± 0.027	65.4	101.3	65.1 ± 14.6

Table 4. Continued.

	E_d (eV)			$\hat{\sigma}_d$ (10^{-21} cm^2 eV)		
Resonance	MCDF[a]	MCBP[a]	Experiment[b,c]	MCDF	MCBP	Experiment[b]
$2s2p^5(^3P_1^o)7l\ (l \geq 4)$	32.096	32.110		213.9	255.0	
$2s2p^5(^1P_1^o)6d$	32.403	32.426		18.3	19.6	
blend	32.120	32.133	32.134 ± 0.009	232.2	274.6	267.2 ± 17.6
$2s2p^5(^1P_1^o)6l\ (l \geq 3)$	34.556	34.571	34.644 ± 0.016	41.8	44.4	42.6 ± 3.0
$2s2p^5(^3P_2^o)8p$	42.833	42.873	42.936 ± 0.010	45.4	47.6	42.0 ± 2.2
$2s2p^5(^3P_2^o)8d$	44.568	44.634	44.684 ± 0.008	78.0	81.4	76.3 ± 2.7
$2s2p^5(^3P_2^o)8l\ (l \geq 3)$	45.453	45.494	45.497 ± 0.001	333.2	317.1	329.3 ± 2.4
$2s2p^5(^3P_1^o)8p$	50.553	50.517	50.612 ± 0.020	17.4	17.9	17.1 ± 2.0
$2s2p^5(^3P_1^o)8d$	52.287	52.277	52.389 ± 0.015	30.8	30.5	28.1 ± 2.1
$2s2p^5(^3P_1^o)8l\ (l \geq 3)$	53.170	53.165	53.310 ± 0.003	140.7	137.3	143.0 ± 2.1
$2s2p^5(^3P_2^o)9p$	58.097	58.133	58.277 ± 0.016	25.7	26.7	22.3 ± 1.6
$2s2p^5(^3P_2^o)9d$	59.276	59.359	59.485 ± 0.011	48.2	46.2	35.7 ± 1.7
$2s2p^5(^3P_2^o)9l\ (l \geq 3)$	59.933	59.969	60.141 ± 0.002	229.7	221.9	210.0 ± 2.4
$2s2p^5(^3P_1^o)9p$	65.793	65.786	65.938 ± 0.031	10.1	10.7	12.9 ± 1.8
$2s2p^5(^3P_1^o)9d$	66.977	67.010	67.239 ± 0.017	18.7	18.1	25.6 ± 1.7
$2s2p^5(^3P_1^o)9l\ (l \geq 3)$	67.649	67.640	67.841 ± 0.005	103.5	101.3	95.7 ± 1.9
$2s2p^5(^3P_2^o)10p$	68.950	68.985	69.150 ± 0.030	17.4	18.0	13.3 ± 1.7
$2s2p^5(^3P_2^o)10d$	69.833	69.871	70.023 ± 0.023	32.5	31.2	23.0 ± 1.8
$2s2p^5(^3P_2^o)10l\ (l \geq 3)$	70.286	70.321	70.534 ± 0.003	182.0	177.7	166.8 ± 2.5
$2s2p^5(^3P_1^o)10p$	76.654	76.643		7.3	7.5	
$2s2p^5(^3P_2^o)11p$	76.941	76.976		13.1	13.4	
blend	76.840	76.857	$76.7 - 77.5$[d]	20.4	20.9	23.2 ± 2.2
$2s2p^5(^3P_2^o)11l\ (l \geq 2)$	77.898	77.934		179.1	176.0	
$2s2p^5(^3P_1^o)10l\ (l \geq 2)$	77.941	77.936		97.1	95.9	
blend	77.913	77.935	$77.5 - 79.0$[d]	276.2	271.9	230.1 ± 2.7
$2s2p^5(^3P_2^o)12p$	82.997	83.031	83.340 ± 0.039	10.5	10.6	9.3 ± 1.2
$2s2p^5(^3P_2^o)12l\ (l \geq 2)$	83.736	83.771	84.036 ± 0.003	156.8	154.9	135.0 ± 1.8
$2s2p^5(^3P_1^o)11p$	84.649	84.637	84.613 ± 0.040	6.6	5.9	10.4 ± 1.4
$2s2p^5(^3P_1^o)11d$	85.307	85.298	85.512 ± 0.096	9.7	9.8	6.2 ± 2.3
$2s2p^5(^3P_1^o)11l\ (l \geq 3)$	85.660	85.649	85.908 ± 0.009	73.0	72.7	71.4 ± 2.4
$2s2p^5(^3P_2^o)13p$	87.629	87.727	87.832 ± 0.063	10.6	8.9	10.3 ± 2.3
$2s2p^5(^3P_2^o)13l\ (l \geq 2)$	88.276	88.310	88.569 ± 0.005	140.6	140.1	127.9 ± 2.8

Table 4. Continued.

	E_d (eV)			$\hat{\sigma}_d$ (10^{-21} cm^2 eV)		
Resonance	MCDF[a]	MCBP[a]	Experiment[b,c]	MCDF	MCBP	Experiment[b]
$2s2p^5(^3P_1^o)12p$	90.706	90.694	91.085 ± 0.105	5.4	4.6	5.5 ± 1.9
$2s2p^5(^3P_2^o)14p$	91.410	91.442		7.6	7.7	
$2s2p^5(^3P_1^o)12l$ $(l \geq 2)$	91.483	91.444		65.6	73.1	
blend	91.475	91.444	91.708 ± 0.012	73.2	80.8	69.2 ± 2.3
$2s2p^5(^3P_2^o)14l$ $(l \geq 2)$	91.877	91.911	92.184 ± 0.007	129.2	128.9	111.3 ± 3.0
$2s2p^5(^3P_2^o)15p$	94.402	94.436	94.636 ± 0.095	6.6	6.7	4.0 ± 1.5
$2s2p^5(^3P_2^o)15l$ $(l \geq 2)$	94.782	94.815	95.083 ± 0.005	118.5	118.7	97.0 ± 1.6
$2s2p^5(^3P_1^o)13p$	95.654	95.393	95.537 ± 0.048	10.4	4.0	10.2 ± 1.5
$2s2p^5(^3P_1^o)13l$ $(l \geq 2)$	96.015	95.982	96.268 ± 0.007	59.6	66.5	57.8 ± 1.4
$2s2p^5(^3P_2^o)16p$	96.845	96.879	96.995 ± 0.079	6.0	6.0	5.5 ± 1.4
$2s2p^5(^3P_2^o)16l$ $(l \geq 2)$	97.158	97.192	97.485 ± 0.005	111.0	111.2	95.5 ± 1.5
$2s2p^5(^3P_2^o)17l$ $(l \geq 1)$	99.127	99.148	99.431 ± 0.010	104.2	110.4	93.3 ± 3.1
$2s2p^5(^3P_1^o)14l$ $(l \geq 1)$	99.610	99.560	99.874 ± 0.015	64.4	64.8	59.9 ± 3.0
$2s2p^5(^3P_2^o)18l$ $(l \geq 0)$	100.76	100.80	101.10 ± 0.01	104.4	105.8	91.7 ± 1.9
$2s2p^5(^3P_2^o)19l$ $(l \geq 0)$	102.16	102.19	102.52 ± 0.02	100.5	100.7	99.9 ± 6.7
$2s2p^5(^3P_1^o)15l$ $(l \geq 1)$	102.50	102.47	102.87 ± 0.03	56.7	60.4	52.2 ± 6.5
$2s2p^5(^3P_2^o)20l$ $(l \geq 0)$	103.35	103.39	103.69 ± 0.01	91.3	95.9	76.5 ± 2.5
$2s2p^5(^3P_2^o)21l$ $(l \geq 0)$	104.38	104.42	104.70 ± 0.02	84.7	83.6	70.6 ± 5.1
$2s2p^5(^3P_1^o)16l$ $(l \geq 1)$	104.87	104.85	105.13 ± 0.05	52.9	56.4	47.0 ± 4.4
$2s2p^5(^3P_2^o)22l$ $(l \geq 0)$	105.27	105.31	105.60 ± 0.02	80.7	79.5	74.6 ± 4.2
$2s2p^5(^3P_2^o)23l$ $(l \geq 0)$	106.05	106.08	106.42 ± 0.01	78.0	76.0	70.9 ± 2.4
$2s2p^5(^3P_2^o)nl$ $(24 \leq n \lesssim 130,\ l \geq 0)$	106.7-114.2			2201.0	2196.8	
$2s2p^5(^3P_1^o)nl$ $(17 \leq n \lesssim 130,\ l \geq 0)$	106.5-121.9			995.0	1031.6	
blend			$106.5 - 123.0$	3196.0	3228.4	2491.9 ± 8.3

[a] Weighted energy: $E_d = \sum_i E_i \hat{\sigma}_i / \sum_i \hat{\sigma}_i$.

[b] 1σ statistical fitting uncertainties only.

[c] Absolute energy scale uncertainty $\lesssim 0.7\%$.

[d] Unable to fit for resonance energy.

Table 5. Experimental and theoretical quantum defects μ_l for Fe XVII and Fe XVIII. Experimental Fe XVII values are determined using Fe XVIII to Fe XVII $\Delta n = 0$ DR via the $^2P_{3/2} -\ ^2P_{1/2}$ and $^2P_{3/2} -\ ^2S_{1/2}$ core excitations. Experimental Fe XVIII values are determined using Fe XIX to Fe XVIII $\Delta n = 0$ DR via the $^3P_2 -\ ^3P_1^o$ and $^3P_2 -\ ^3P_2^o$ core excitations. The 1σ statistical fitting uncertainties are given. Experimental results are for ions with an excited core configuration. Theoretical values are from Theodosiou, Inokuti, & Manson (1986) and are for ions with a ground state core configuration.

	Fe XVII			Fe XVIII		
l	$^2P_{3/2} -\ ^2P_{1/2}$	$^2P_{3/2} -\ ^2S_{1/2}$	Theory	$^3P_2 -\ ^3P_1^o$	$^3P_2 -\ ^3P_2^o$	Theory
s	0.2762 ± 0.0006		0.2616			
p	0.1786 ± 0.0009	0.1811 ± 0.0003	0.1718	0.1455 ± 0.0025	0.1455 ± 0.0022	0.1460
d	0.0612 ± 0.0013	0.0679 ± 0.0002	0.0573	0.0441 ± 0.0039	0.0478 ± 0.0024	0.0502

Table 6. Fit parameters for the experimentally inferred and theoretical MCDF Fe XVIII to Fe XVII and Fe XIX to Fe XVIII $\Delta n = 0$ DR rate coefficients. The units for c_i are cm^3 s^{-1} K$^{1.5}$ and for E_i are eV.

	Fe XVIII				Fe XIX			
	Experiment		MCDF		Experiment		MCDF	
i	c_i	E_i	c_i	E_i	c_i	E_i	c_i	E_i
1	4.79e-6	2.22e-1	5.55e-6	2.15e-1	3.73e-5	6.61e-2	3.16e-5	6.19e-2
2	9.05e-5	5.24e-1	7.37e-5	5.36e-1	1.60e-5	2.14e-1	2.14e-5	1.94e-1
3	3.48e-5	1.16e+0	7.47e-5	1.95e+0	2.33e-4	1.11e+0	2.77e-4	1.09e+0
4	1.83e-4	2.52e+0	2.06e-4	3.79e+0	3.63e-4	2.60e+0	3.97e-4	2.50e+0
5	5.26e-4	6.57e+0	6.64e-4	1.17e+1	1.16e-3	6.54e+0	1.43e-3	6.78e+0
6	2.12e-3	1.90e+1	1.27e-3	2.18e+1	5.56e-3	2.53e+1	5.85e-3	2.63e+1
7	4.29e-3	5.66e+1	5.78e-3	6.40e+1	4.12e-2	9.70e+1	5.18e-2	1.00e+2
8	3.16e-2	1.21e+2	3.03e-2	1.26e+2				

REFERENCES

Aldrovandi, S. M. V. & Péquignot, D. 1973, A&A, 25, 137; 1976, A&A, 47, 321

Angelini, L., White, N. E., Nagase, F., Kallman, T. R., Yoshida, A., Takeshima, Becker, C., & Paerels, F. 1995, ApJ, 449, L41

Arnaud, M. & Rothenflug, R. 1985, A&AS, 60, 425

Arnaud, M. & Raymond, J. 1992, ApJ, 398, 394

Badnell, N. R. 1986, J. Phys. B, 19, 3827

Badnell, N. R. 1997, J. Phys. B, 30, 1

Burgess, A. 1965, ApJ, 141, 1588

Chen, M. H. 1985, Phys. Rev. A, 31, 1449

Chen, M. H. 1988, Phys. Rev. A, 38, 2332

Cheng, K. T., Kim, Y.-K., & Desclaux, J. P. 1979, At. Data Nucl. Data Tables, 24, 111

Corliss, C. & Sugar, J. 1982, J. Phys. Chem. Ref. Data, 11, 135

Dasgupta, A. & Whitney, K. G. 1990, Phys. Rev. A, 42, 2640

Dasgupta, A. & Whitney, K. G. 1994, At. Data Nucl. Data Tables, 58, 77

DeWitt, D. R. et al. 1996, Phys. Rev. A, 53, 2327

Fuhr, J. R., Martin, G. A., & Wiese, W. L. 1988, J. Phys. Chem. Ref. Data, 17, Suppl. No. 4

Grant, I. P., McKenzie, B. J., Norrington, P. H., Mayers, D. F., & Pyper, N. C. 1980, Comput. Phys. Commun., 21, 207

Grieser, M. et al. 1991 in Cooler Rings and Their Applications, ed. T. Katayama & A. Noda, (World Scientific: Singapore), 190

Habs, D. et al. 1989, Nucl. Instrum. Methods, B43, 390

Hahn, Y. 1993, J. Quant. Spectrosc. Radiat. Transfer, 49, 81

Hess, C. J., Kahn, S. M., & Paerels, F. B. S. 1997, ApJ, 478, 94

Hochadel, B., Albrecht, F., Grieser, M., Habs, D., Schwalm, D., Szmola, E., and Wolf, A. 1994, Nucl. Instrum. Methods, A343, 401

Hoffknecht, A. et al. 1998, J. Phys. B, 31, 2415

Kahn, S. M. & Liedahl, D. A. 1995, in Physics of Multiply Charged Ions, ed. D. Liesen (Plenum Press: New York), 169

Kallman, T. R., Liedahl, D., Osterheld, A., Goldstein, W., and Kahn, S. 1996, ApJ, 465, 994

Kallman, T. R. & Krolik, J. H. 1997, XSTAR, A Spectral Analysis Tool.

Kelly, R. L. 1987, J. Phys. Chem. Ref. Data, 16, Suppl. 1

Kilgus, G., Habs, D., Schwalm, D., Wolf, A., Badnell, N. R., and Müller, A. 1992, Phys. Rev. A, 46, 5730

Lampert, A., Wolf, A., Habs, D., Kilgus, G., Schwalm, D., Pindzola, M. S., and Badnell, N. R. 1996, Phys. Rev. A, 53, 1413

Liedahl, D. A., Kahn, S. M., Osterheld, A. L., & Goldstein, W. H. 1990, ApJ, 350, L37

Liedahl, D. A. 1992, Ph. D. Thesis, University of California at Berkeley

Liedahl, D. A. & Paerels, F. 1996, ApJ, 468, L33

Linkemann, J. et al. 1995, Nucl. Instrum. Methods, B98, 154

Marxer, H. & Spruch, L. 1991, Phys. Rev. A, 43, 1268

Miersch, G., Habs, D., Kenntner, J., Schwalm, D., & Wolf, A. 1996, Nucl. Instrum. Methods A, 369, 277

Nahar, S. N. 1997, Phys. Rev. A, 55, 1980

Nahar, S. N. & Pradhan, A. K. 1994, Phys. Rev. A, 49, 1816

Nahar, S. N. & Pradhan, A. K. 1995, ApJ, 447, 966

Nussbaumer, H. & Storey, P. J. 1983, A&A, 126, 75

Pastuszka, S. et al. 1996, Nucl. Instrum. Methods A, 369, 11

Poth, H. 1990, Phys. Rep. 196, 135

Reynolds, C. S. & Fabian, A. C. 1995, MNRAS, 273, 1167

Roszman, L. J. 1987a, Phys. Rev. A, 35, 2138

Roszman, L. J. 1987b, Phys. Rev. A, 35, 3368

Savin, D. W. et al. 1997, ApJ, 489, L115

Savin, D. W. et al. 1998, in NIST Special Publications 926, Poster Papers, International Conference on Atomic and Molecular Data and Their Applications (ICAMDATA 97), ed. W. L. Wiese & P. J. Mohr, (U.S. Government Printing Office, Washington), 96

Seaton, M. J. & Storey, P. J. 1976, in Atomic Processes and Applications, ed. P. G. Burke & B. L. Moisewitch (North-Holland, Amsterdam), 133

Schippers, S., Bartsch, T., Brandau, C., Gwinner, G., Linkemann, J., Müller, A., Saghiri, A. A., and Wolf, A. 1998, J. Phys. B, 31, 4873

Shirai, T., Funatake, Y., Mori, K., Sugar, J., Wiese, W. L., & Nakai, Y. 1990, J. Phys. Chem. Ref. Data, 19, 127

Shull, J. M. & Van Steenberg, M. 1982, ApJS, 48, 95; 49, 351

Sugar, J. & Corliss, C. 1985, J. Phys. Chem. Ref. Data, 24, Suppl. No. 2

Theodosiou, C. E., Inokuti, M., & Manson, S. T. 1986, At. Data Nucl. Data Tables, 35, 473

This preprint was prepared with the AAS LaTeX macros v4.0.

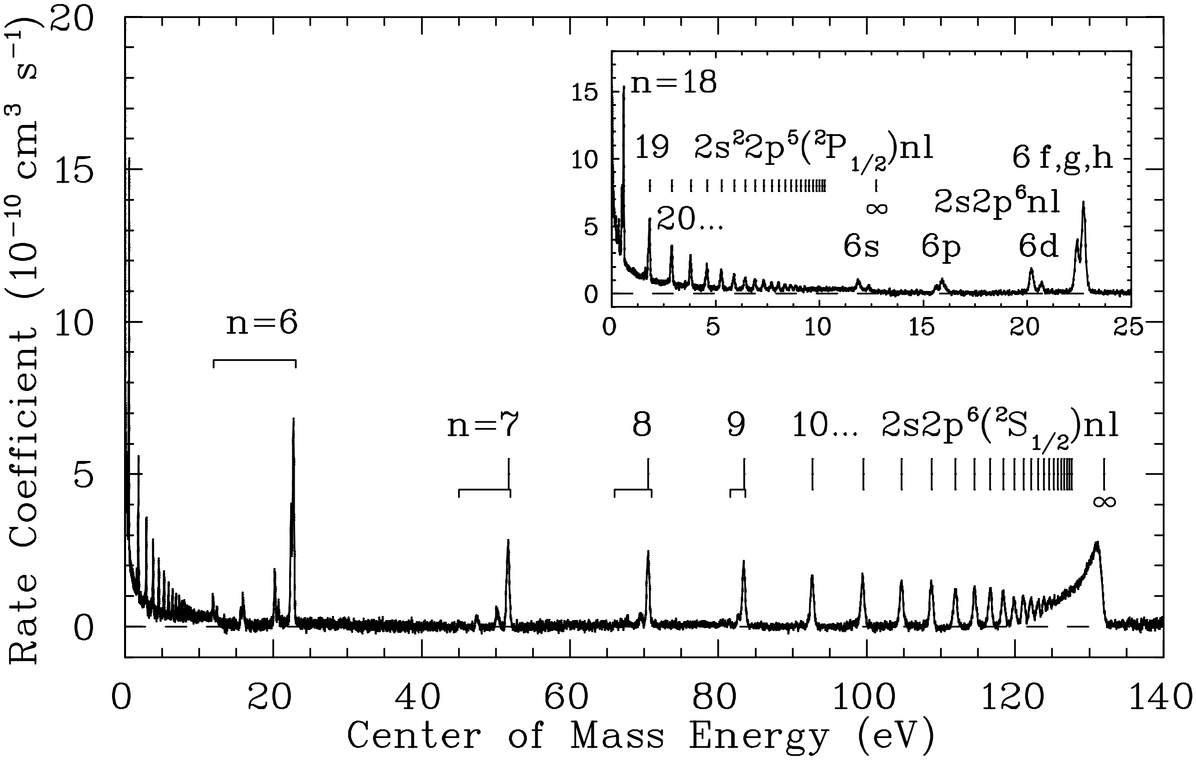

Fig. 1.— Measured Fe XVIII to Fe XVII recombination rate coefficient versus electron-ion collision energy. $\Delta n = 0$ DR resonances resulting from $^2P_{3/2} -\ ^2P_{1/2}$ and $^2P_{3/2} -\ ^2S_{1/2}$ core excitations are labeled. The nonresonant "background" rate is due primarily to RR with some residual CT (see text).

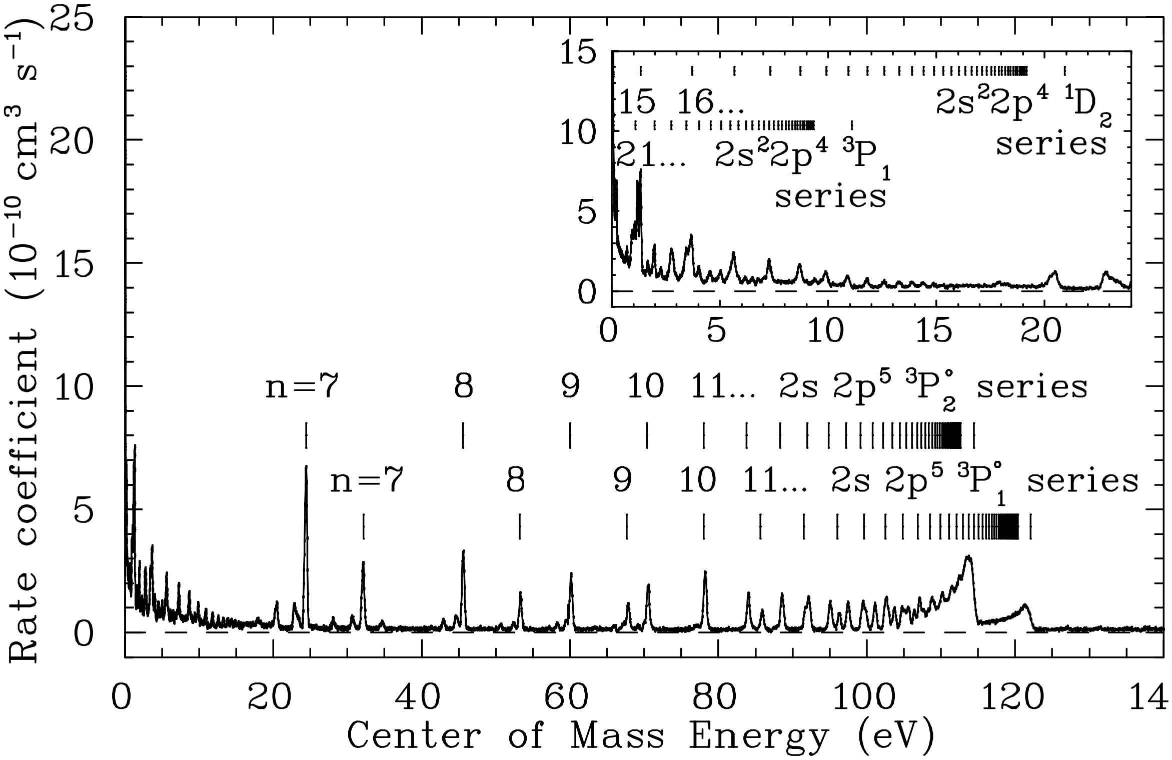

Fig. 2.— Measured Fe XIX to Fe XVIII recombination rate coefficient versus electron-ion collision energy. $\Delta n = 0$ DR resonances resulting from $^3P_2 - \,^3P_1$, $^3P_2 - \,^1D_2$, $^3P_2 - \,^3P_2^o$, and $^3P_2 - \,^3P_1^o$ core excitations are labeled for capture into high l levels. The nonresonant "background" rate is due primarily to RR with some residual CT (see text).

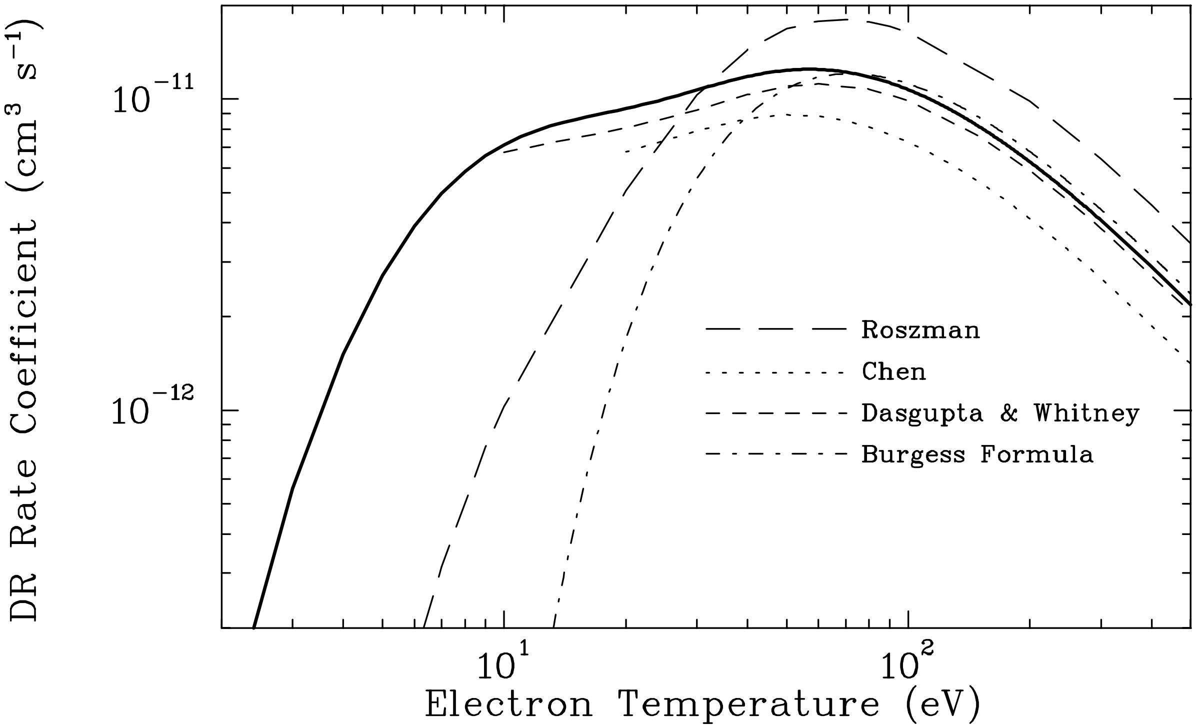

Fig. 3.— Fe XVIII to Fe XVII Maxwellian-averaged rate coefficients for $\Delta n = 0$ DR via $^2P_{3/2} - {}^2S_{1/2}$ core excitations. The thick solid line is the integration of the experimental DR resonance strengths and energies extracted from the results shown in Figure 1 and listed in Table 3. There is an estimated $\lesssim 20\%$ total systematic uncertainty in our experimentally inferred rate. Calculations are from Roszman (1987a; long-dashed curve), Chen (1988; dotted curve), Dasgupta & Whitney (1990; short-dashed curve) and the Burgess formula (1965; short-dashed-dot curve).

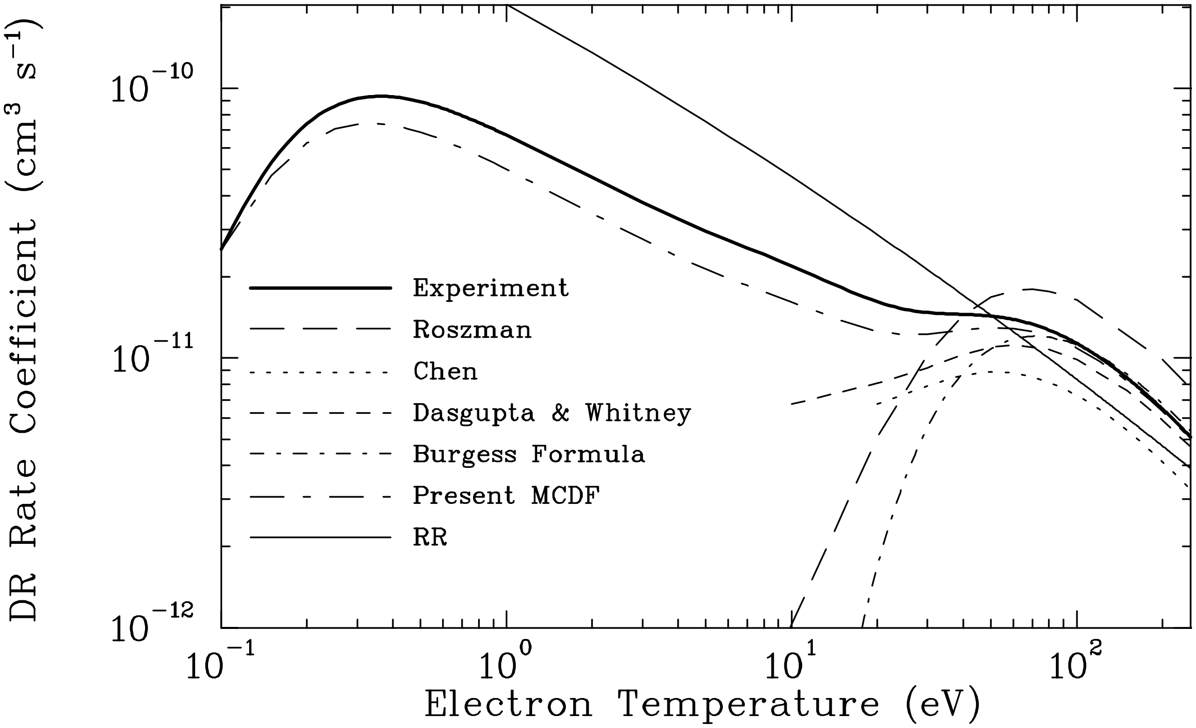

Fig. 4.— Fe XVIII to Fe XVII Maxwellian-averaged $\Delta n = 0$ DR total rate coefficients. The thick solid curve is the integration of the experimental DR resonance strengths and energies extracted from the results shown in Figure 1 and listed in Tables 2 and 3. There is an estimated $\lesssim$ 20% total systematic uncertainty in our experimentally inferred rate. Existing calculations by Roszman (1987a; long-dashed curve), Chen (1988; dotted curve), Dasgupta & Whitney (1990; short-dashed curve) and the Burgess formula (1965; short-dashed-dot curve) do not include the ${}^2P_{3/2} - {}^2P_{1/2}$ DR channel. The long-dashed-dot curve shows the results of our new MCDF calculations which include this channel. Our MCBP rate (not shown here) agrees well with our MCDF rate. The thin solid curve shows the recommended RR rate of Arnaud & Raymond (1992).

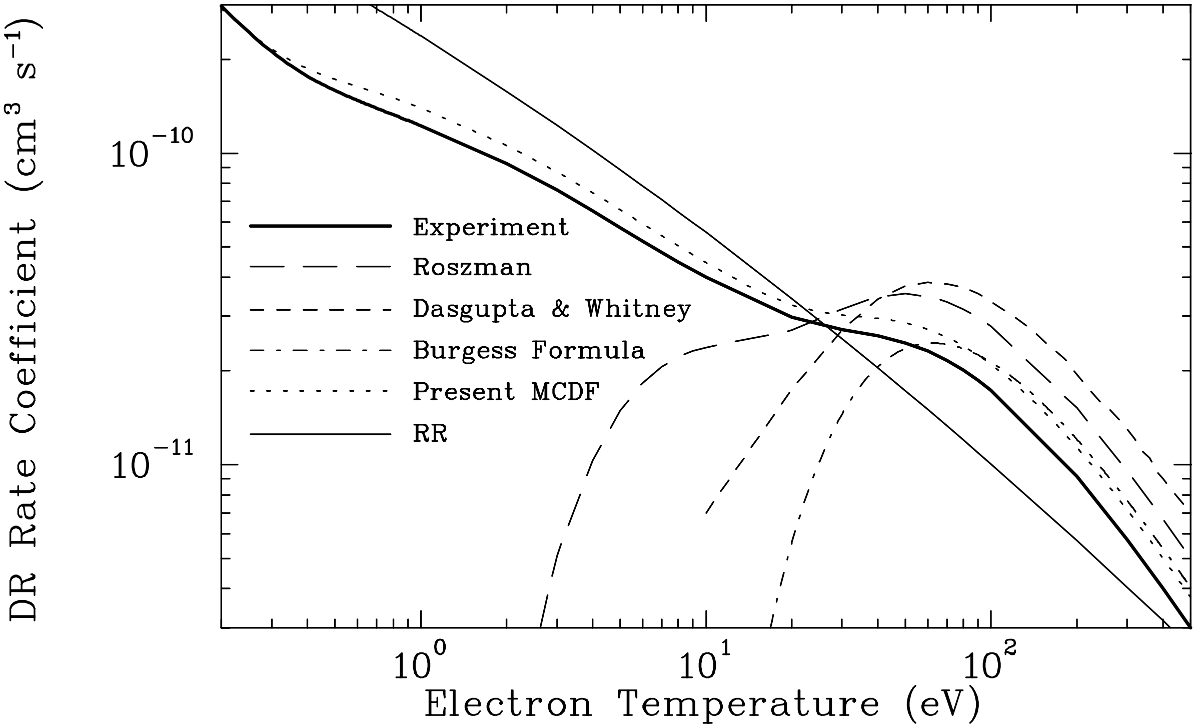

Fig. 5.— Fe XIX to Fe XVIII Maxwellian-averaged $\Delta n = 0$ DR rate coefficients. The thick solid line is calculated using the measured DR resonance strengths and energies extracted from the results shown in Figure 2 and listed in Table 4. There is an estimated $\lesssim 20\%$ total systematic uncertainty in our experimentally inferred rate. Also shown are existing theoretical calculations by Roszman (1987b; long-dashed curve) and Dasgupta & Whitney (1994; short-dashed curve), the Burgess formula (1965; short-dashed-dot curve) and our new MCDF calculations (dotted curve). Our MCBP rate (not shown here) agrees well with our MCDF rate. The thin solid curve shows the recommended RR rate of Arnaud & Raymond (1992).

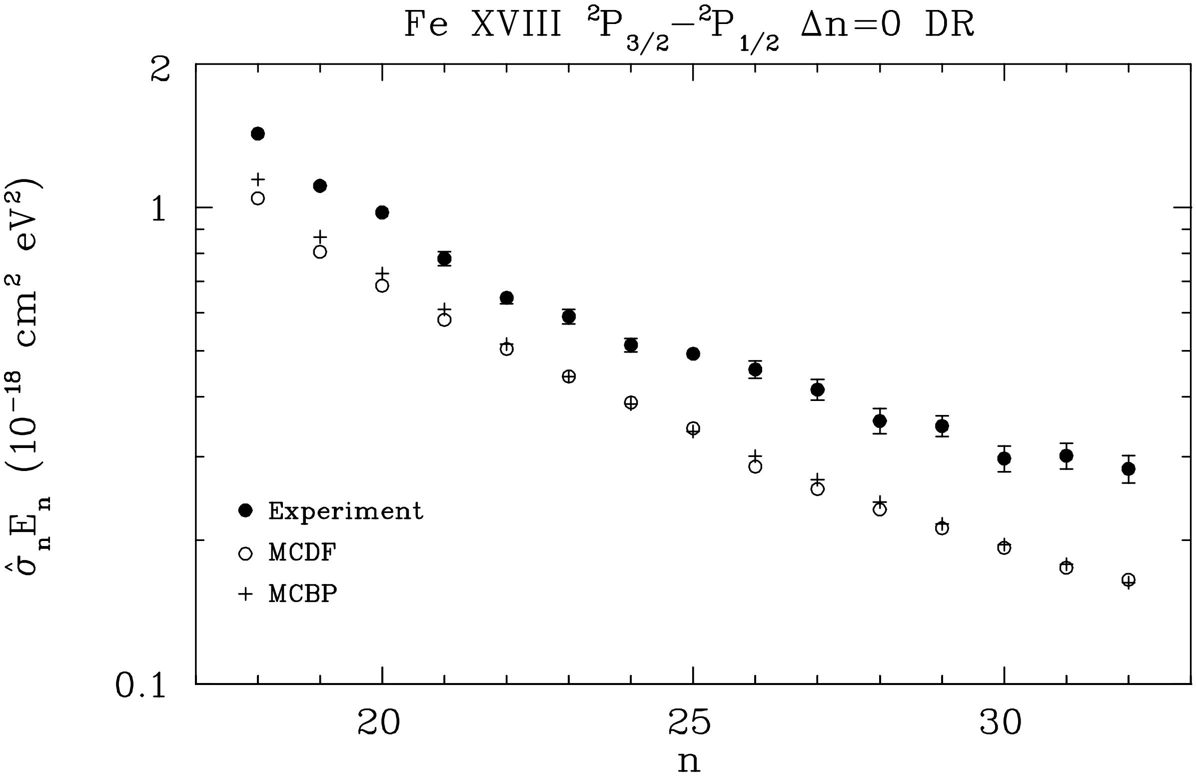

Fig. 6.— DR resonance strength $\hat{\sigma}_n E_n$ as a function of the principal quantum number n for Fe XVIII to Fe XVII $\Delta n = 0$ DR via the ${}^2P_{3/2} - {}^2P_{1/2}$ core excitation. There is an estimated $\lesssim 20\%$ total systematic uncertainty in our experimental values (at a 90% confidence level). Filled circles are the present experimental results. Error bars represent the 1σ statistical fitting uncertainties. Open circles are our MCDF calculations and crosses are our MCBP calculations.

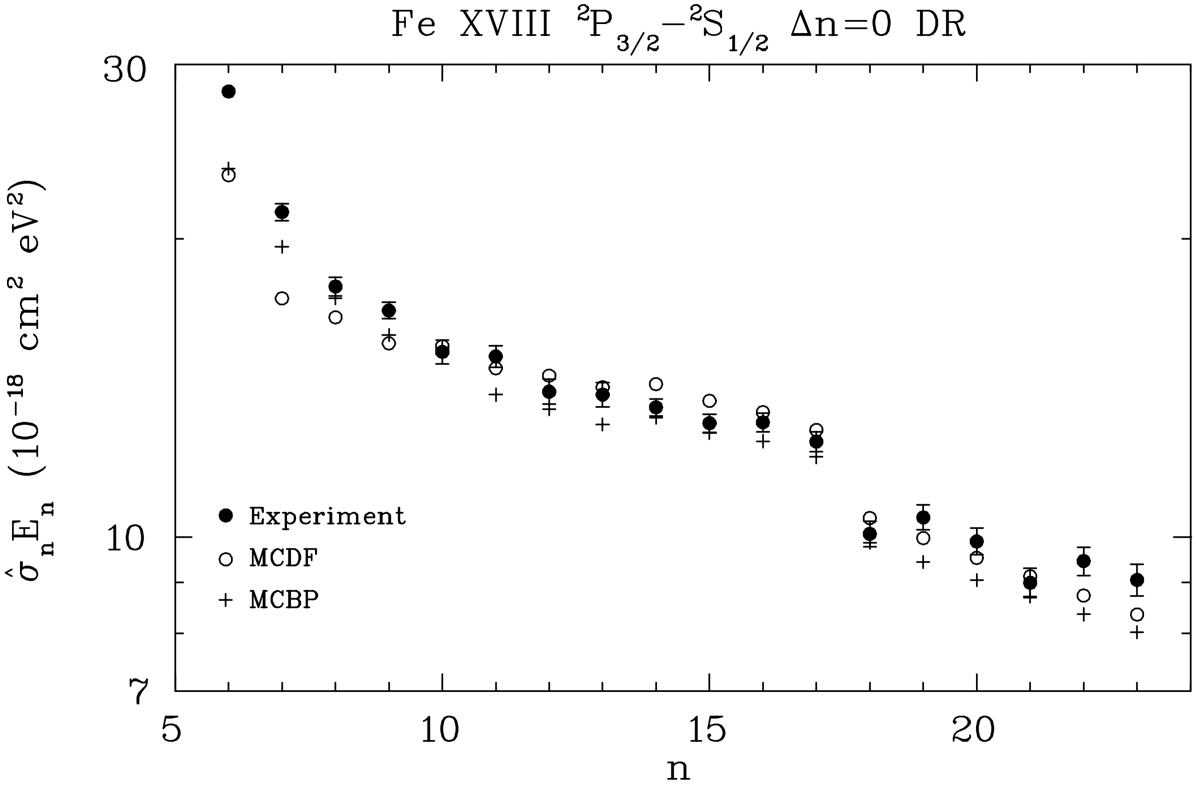

Fig. 7.— DR resonance strength $\hat{\sigma}_n E_n$ as a function of the principal quantum number n for Fe XVIII to Fe XVII $\Delta n = 0$ DR via the $^2P_{3/2} - \,^2S_{1/2}$ core excitation. See Figure 6 for further details.

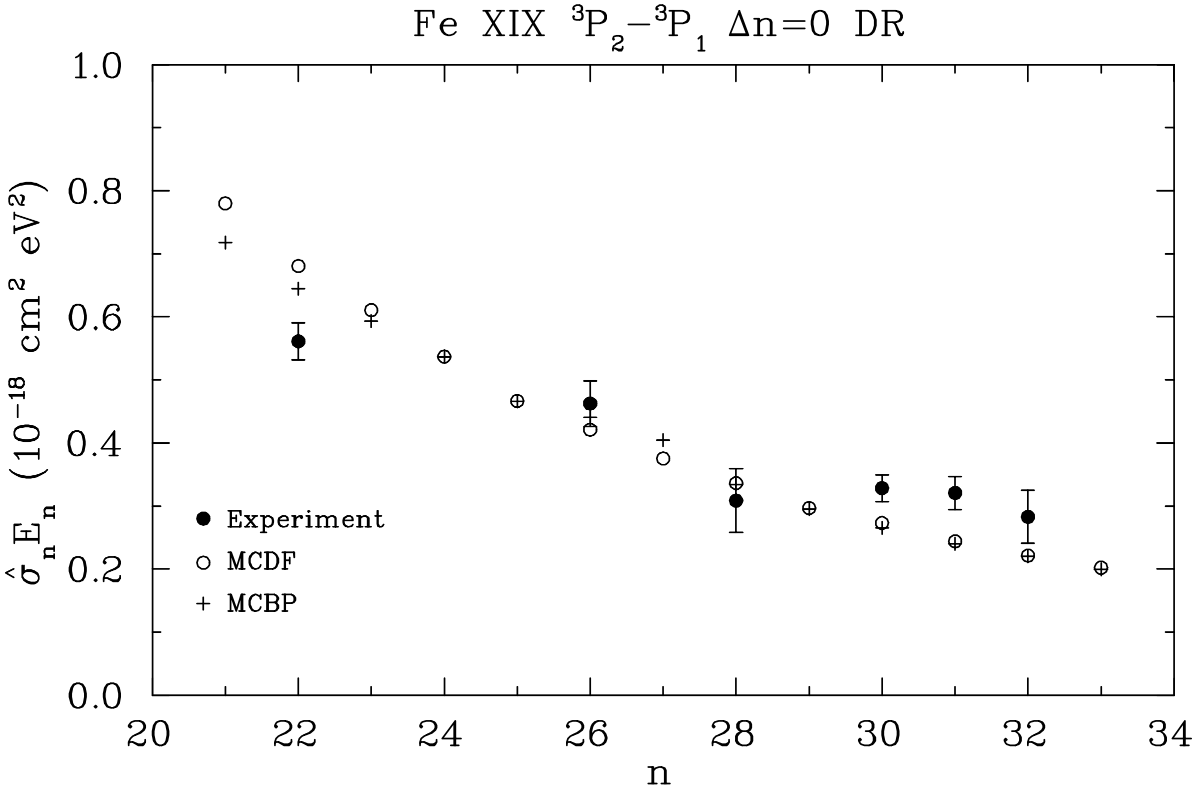

Fig. 8.— DR resonance strength $\hat{\sigma}_n E_n$ as a function of the principal quantum number n for Fe XIX to Fe XVIII $\Delta n = 0$ DR via the $^3P_2 - {}^3P_1$ core excitation. See Figure 6 for further details.

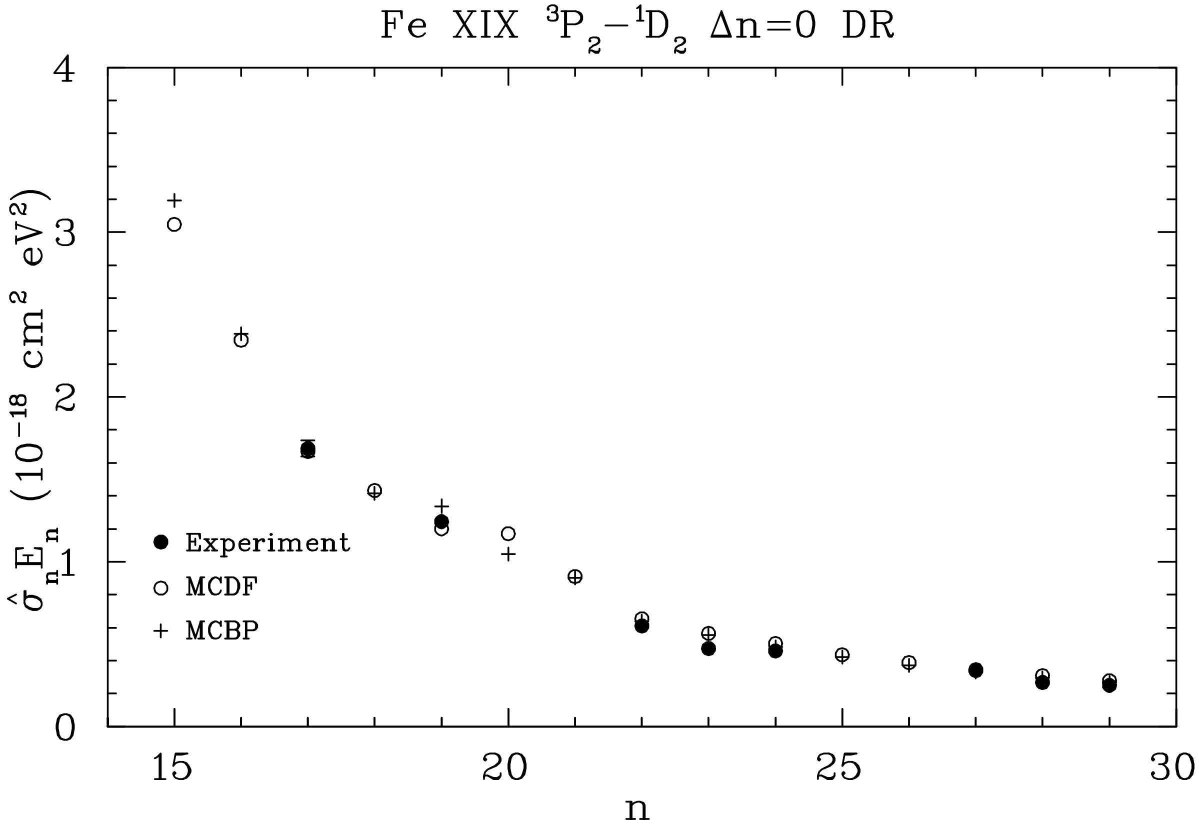

Fig. 9.— DR resonance strength $\hat{\sigma}_n E_n$ as a function of the principal quantum number n for Fe XIX to Fe XVIII $\Delta n = 0$ DR via the $^3P_2 - {}^1D_2$ core excitation. See Figure 6 for further details.

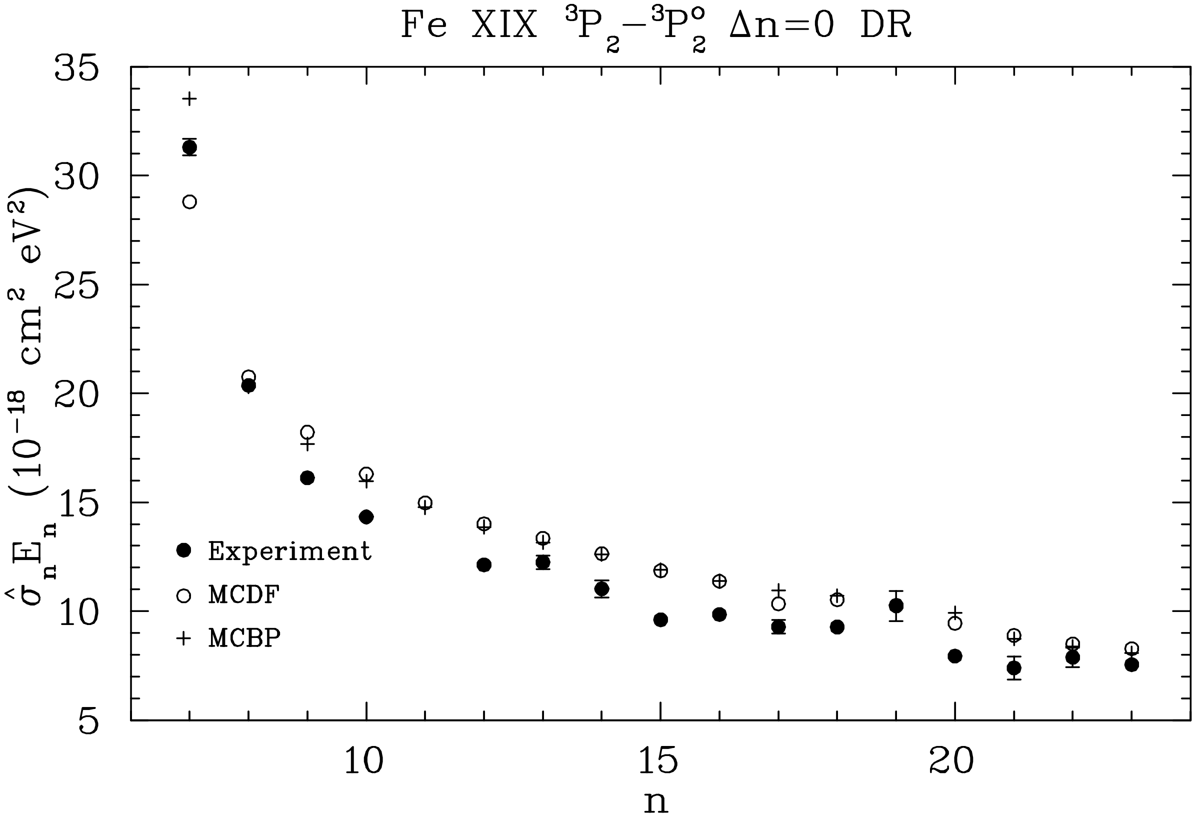

Fig. 10.— DR resonance strength $\hat{\sigma}_n E_n$ as a function of the principal quantum number n for Fe XIX to Fe XVIII $\Delta n = 0$ DR via the $^3P_2 - {}^3P_2^o$ core excitation. See Figure 6 for further details.

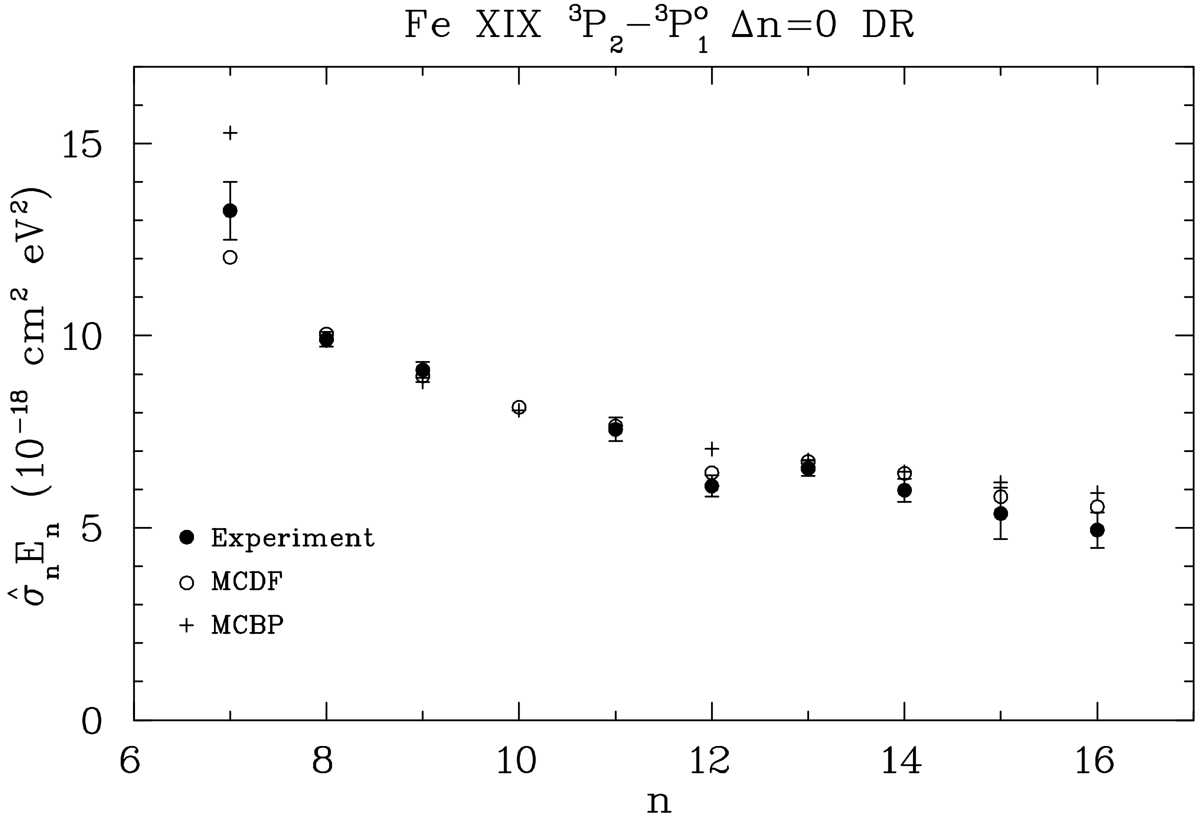

Fig. 11.— DR resonance strength $\hat{\sigma}_n E_n$ as a function of the principal quantum number n for Fe XIX to Fe XVIII $\Delta n = 0$ DR via the $^3P_2 -\ ^3P_1^o$ core excitation. See Figure 6 for further details.

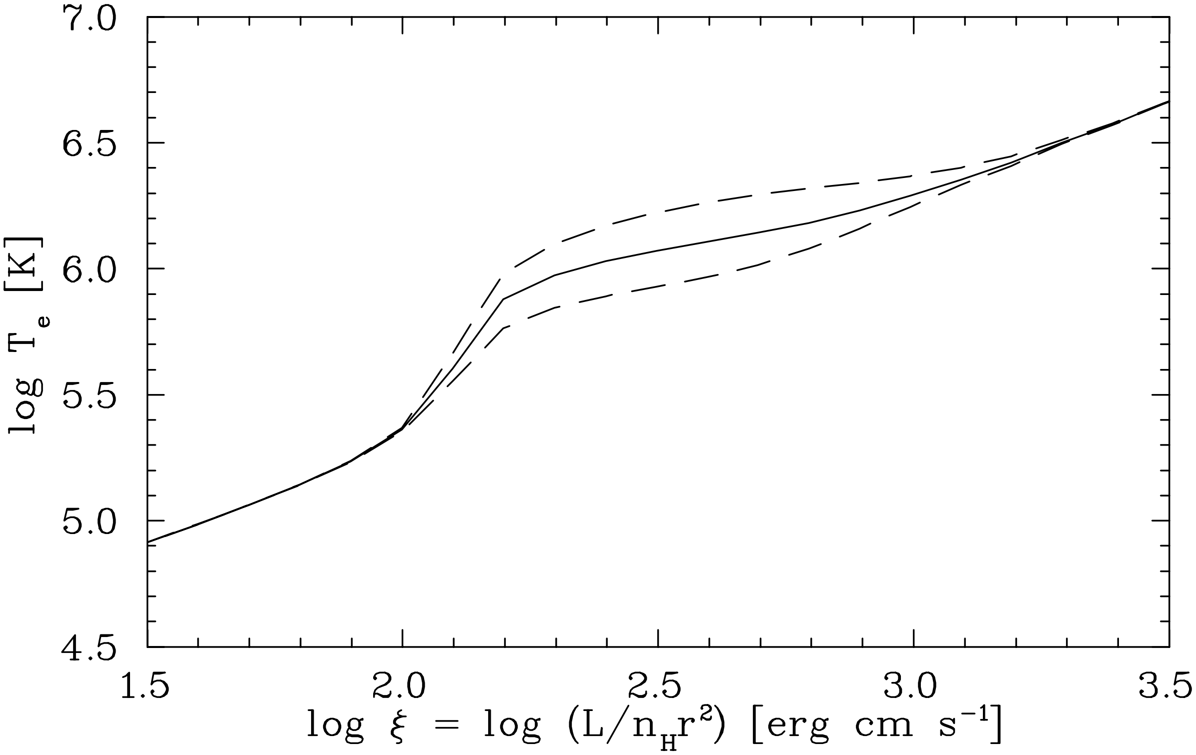

Fig. 12.— Predicted electron temperature versus ionization parameter ξ for a model AGN ionizing spectrum illuminating a slab of gas with cosmic abundances. The solid curve shows the predicted T_e using our inferred Fe XVIII and Fe XIX DR rates and the unchanged $\Delta n = 0$ DR rates for Fe XX through Fe XXIV. The upper(lower) dashed curve results when the $\Delta n = 0$ DR rates for Fe XX through Fe XXIV are increased(decreased) by a factor of 2.

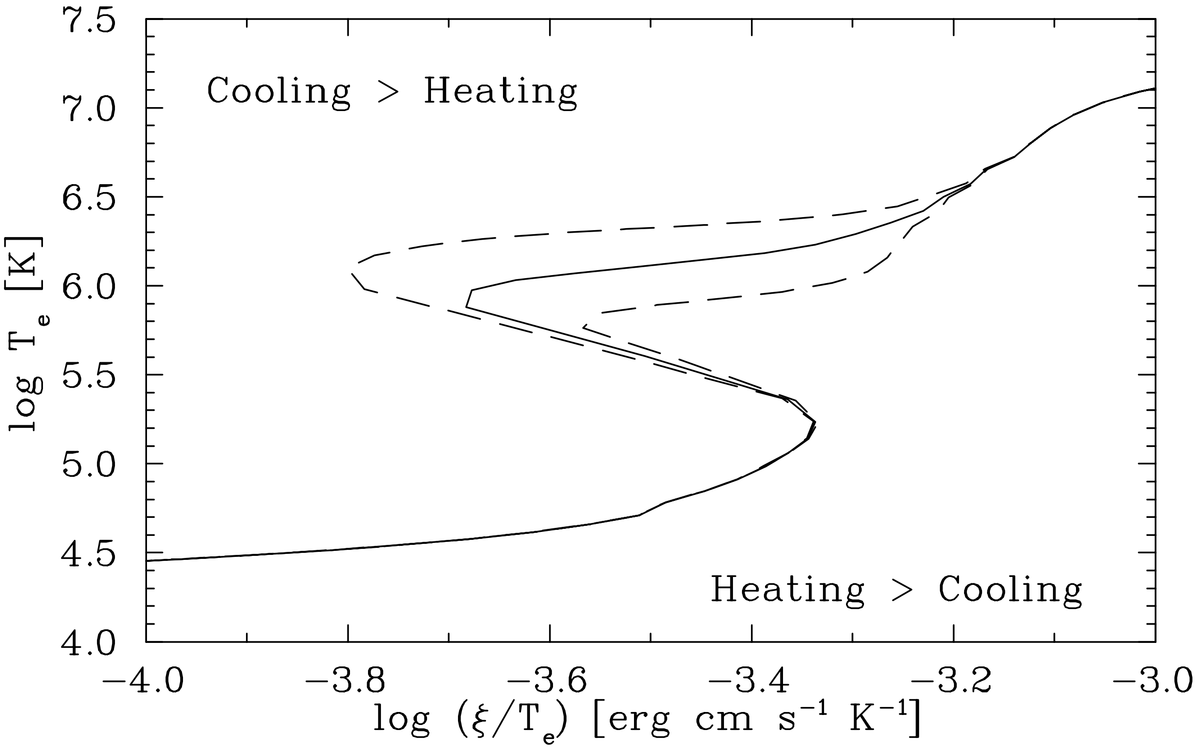

Fig. 13.— Predicted electron temperature versus ξ/T_e for a model AGN ionizing spectrum illuminating a slab of gas with cosmic abundances. The solid curve shows the predicted T_e using our inferred Fe XVIII and Fe XIX DR rates and the unchanged $\Delta n = 0$ DR rates for Fe XX through Fe XXIV. The upper(lower) dashed curve results when the $\Delta n = 0$ DR rates for Fe XX through Fe XXIV are increased(decreased) by a factor of 2.